bioRxiv preprint doi: https://doi.org/10.1101/2020.08.28.271742; this version posted August 30, 2020. The copyright holder for this preprint (which was not certified by peer review) is the author/funder, who has granted bioRxiv a license to display the preprint in perpetuity. It is made available under aCC-BY-ND 4.0 International license.

# Spontaneous single synapse activity predicts evoked neurotransmission by using overlapping machinery

Both neurotransmission modes use similar machinery

Andreas T. Grasskamp[1], Meida Jusyte[1,2], Anthony W. McCarthy[1], Torsten W.B. Götz[1], Alexander M. Walter[1,2,*]

[1]*Leibniz-Forschungsinstitut für Molekulare Pharmakologie, Robert-Rössle-Straße 10, 13125 Berlin, Germany*

[2]*Einstein Center for Neurosciences, Charité Universitätsmedizin Berlin, Charitéplatz 1, 10117 Berlin, Germany*

**Corresponding author: awalter@fmp-berlin.de (A.M.W.)*

*Charité CrossOver, Charitéplatz 1/Virchowweg 6, 10117 Berlin*

*ORCID: 0000-0002-5895-6529 (A.T.G.) 0000-0001-9948-871X (M.J.) 0000-0002-3771-351X (A.W.M.) 0000-0001-5646-4750 (A.M.W.)*

## Abstract

Synaptic transmission relies on presynaptic neurotransmitter (NT) release from synaptic vesicles (SVs), and on NT detection by postsynaptic receptors. Two principal modes exist: action-potential (AP) evoked and AP-independent "spontaneous" transmission. Though universal to all synapses and essential for neural development and function, regulation of spontaneous transmission remains enigmatic. Mechanisms divergent from AP-evoked transmission were described, but are difficult to reconcile with its established function in adjusting AP-evoked transmission. By studying neurotransmission at individual synapses of *Drosophila* larval neuromuscular junctions (NMJs), we show a clear interdependence of transmission modes: Components of the AP-evoked NT-release machinery (Unc13, Syntaxin-1 and BRP) also predicted spontaneous transmission. Both modes were reduced when blocking voltage-gated calcium channels and engaged an overlapping pool of SVs and NT-receptors. While a small subset (~21%) of spontaneously active synapses

bioRxiv preprint doi: https://doi.org/10.1101/2020.08.28.271742; this version posted August 30, 2020. The copyright holder for this preprint (which was not certified by peer review) is the author/funder, who has granted bioRxiv a license to display the preprint in perpetuity. It is made available under aCC-BY-ND 4.0 International license.

appeared limited to this mode, most also mediated AP-evoked transmission and activity was highly correlated. Thus, by engaging overlapping molecular machinery, spontaneous transmission predicts AP-evoked transmission at single synapses.

## Introduction

Synaptic transmission relies on quantal neurotransmitter (NT) release from synaptic vesicles (SVs) fusing with the plasma membrane at presynaptic active zones (AZs) and subsequent NT detection at postsynaptic receptors (1). Transmission is evoked by APs but also occurs "spontaneously" without AP stimuli (2–4). While AP-evoked NT release is well characterized and vital for neural communication, spontaneous transmission guides synapse development, excitability, homeostasis and plasticity (5) but regulatory mechanisms remain elusive.

APs depolarize the membrane potential, inducing voltage-gated $Ca^{2+}$ channel (VGCCs) opening and $Ca^{2+}$-influx. $Ca^{2+}$ binding to the SV-associated $Ca^{2+}$ sensor synaptotagmin-1 (Syt-1) causes SV fusion (6, 7) via the formation of the neuronal SNARE complex between vesicular Synaptobrevin and the plasma membrane SNAP-25 and syntaxin-1/Syx-1 proteins (7–10). NT release further requires the SNARE-binding proteins (M)Unc13 and (M)Unc18 (11, 12). AZ cytomatrix proteins like Rab3-interacting molecule (RIM), RIM-binding protein (RBP), and ELKS/Bruchpilot (BRP) contribute to AP-evoked transmission by organizing this release machinery (13–15).

Loss of Syt-1 or the SNARE-binding protein complexin (16, 17) decreases AP-evoked transmission rates and increases spontaneous transmission in *Drosophila* and *C. elegans*, arguing for dual function in promoting AP-–evoked and clamping spontaneous transmission (18–22). Yet, whether the clamping function is conserved in mammals is debated (17, 19, 20, 22–29). However,

bioRxiv preprint doi: https://doi.org/10.1101/2020.08.28.271742; this version posted August 30, 2020. The copyright holder for this preprint (which was not certified by peer review) is the author/funder, who has granted bioRxiv a license to display the preprint in perpetuity. It is made available under aCC-BY-ND 4.0 International license.

in the presence of Syt-1/complexin, spontaneous transmission is promoted by the same Syt-1 $Ca^{2+}$ binding sites that mediate AP-evoked release (30) and mutations in SNAP25 or titration of Syx-1 levels affect both transmission modes, consistent with using the same release machinery (30, 31). Yet other studies identified a distinct machinery for spontaneous transmission, with its own $Ca^{2+}$ sensor (Doc2) (32, 33)(alternative function in 34) and SNAREs (35–39). Thus, while genetic interference studies can be useful to study gene function, they provided conflicting results regarding both transmission modes. This could be due to compensatory/homeostatic responses, and studying wildtype synapses of varying composition and function could, in principle, circumvent this. This is the case at the developing synapses of the larval *Drosophila* NMJ (40–43).

Spontaneous NT release increases with intracellular $Ca^{2+}$ while exogenous $Ca^{2+}$ buffers diminish it (44, 33, 45). Accordingly, spontaneous $Ca^{2+}$ influx through VGCCs or release from internal stores may drive spontaneous transmission (46–50). However, unlike in mammals, spontaneous activity at the *Drosophila* NMJ does not depend on extracellular $Ca^{2+}$ ($[Ca^{2+}]_{ext.}$) (22, 51) for unknown reasons.

It is further debated whether the same (52–54, 45) or distinct (55–57) SV pools engage in both transmission modes. Pharmacological experiments with use-dependent receptor blockers demonstrated segregated activation of NT receptors (58, 42, 59), but some interdependence was seen and is needed for synaptic homeostasis (60). Live imaging experiments reported on a spatial segregation of transmission modes (42) while other studies found significant overlap (41, 61). A lack of positive correlation and an independent regulation of the two transmission modes were reported in these cases.

bioRxiv preprint doi: https://doi.org/10.1101/2020.08.28.271742; this version posted August 30, 2020. The copyright holder for this preprint (which was not certified by peer review) is the author/funder, who has granted bioRxiv a license to display the preprint in perpetuity. It is made available under aCC-BY-ND 4.0 International license.

We here report on interdependences between spontaneous and AP-evoked neurotransmission at single synapses of the wildtype *Drosophila melanogaster* NMJ. Our data reconcile previous reports on both dedicated and overlapping transmission modes. However, we show that the majority of AZs engage in both transmission modes, and that correct assessment relies heavily on the experimental paradigm. Both AP-evoked and spontaneous transmission capitalize on an overlapping molecular machinery and are highly correlated. We thus propose that spontaneous activity serves as a scalable, highly uniform readout ("ping") of connectivity strength for synapse maturation, maintenance, and plasticity.

## Results & Discussion

### Presynaptic AZ protein levels predict NT release modes

Addressing relations between spontaneous and AP-evoked transmission modes is hampered by the difficulty to assess them at the same synapse. We used a live-imaging approach to track synaptic activity at the *Drosophila* 3$^{rd}$ instar larval NMJ (type Ib boutons of muscle 4) by postsynaptically expressing the fluorescent $Ca^{2+}$-reporter GCaMP5 (**Fig. 1 A**). Presynaptic glutamate release opens postsynaptic ionotropic receptors which are permeable to $Ca^{2+}$, leading to postsynaptic $Ca^{2+}$-influx and GCaMP fluorescence increase (**Fig. 1 B&I**) (62, 41). Rapid $Ca^{2+}$ dispersion in the muscle limits spatial signal resolution: Individual events were well approximated with a Gaussian (**Fig. 1 C**) and comparing signals across cells revealed a mean resolution (Full Width at Half Maximum, FWHM) of 1.72 µm. To relate this to inter-AZ distances at the NMJ, we identified AZ-locations in confocal imaging by post-hoc immunohistochemical (IHC) staining against the AZ protein BRP (63) (**Fig. 1 D**). Most AZ pairs were far enough apart to distinguish the signals (**Fig. 1 E-G**). However, proximal AZs were closer than the FWHM of the GCaMP signal (nearest

bioRxiv preprint doi: https://doi.org/10.1101/2020.08.28.271742; this version posted August 30, 2020. The copyright holder for this preprint (which was not certified by peer review) is the author/funder, who has granted bioRxiv a license to display the preprint in perpetuity. It is made available under aCC-BY-ND 4.0 International license.

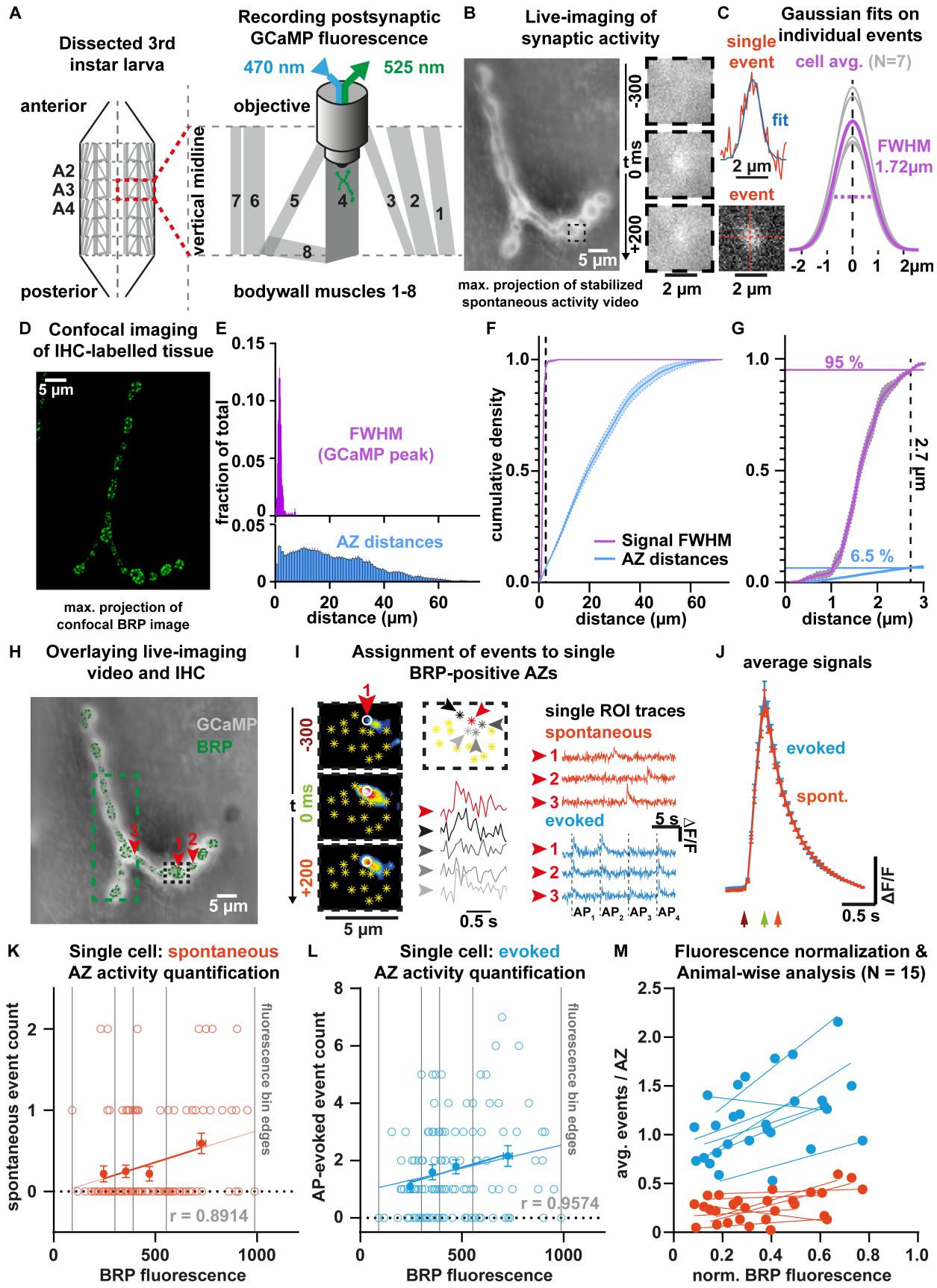


91

bioRxiv preprint doi: https://doi.org/10.1101/2020.08.28.271742; this version posted August 30, 2020. The copyright holder for this preprint (which was not certified by peer review) is the author/funder, who has granted bioRxiv a license to display the preprint in perpetuity. It is made available under aCC-BY-ND 4.0 International license.

**Figure 1 Postsynaptic fluorescence measurements of presynaptic activity with single AZ precision.** (**A**) Quantification of $Ca^{2+}$ induced fluorescence signals in *Drosophila* larvae postsynaptically expressing GCaMP. (**B**) Left: Contrast adjusted maximal projection of stabilized 100 s spontaneous activity video; Right: 500ms time sequence of single event observed in indicated ROI (**C**) Gaussian fits on 532 individual spontaneous events determined the spatial spread of GCaMP events. Cell-wise (N =7 animals) FWHM was 1.722±0.018 µm, , mean±SEM (purple). Lower left: contrast adjusted maximal projection of single event (6 frames) (**D**) IHC (anti-BRP) labelled NMJ from (**B**). (**E**) Histograms of FWHM (purple) and AZ distances (blue) (**F**) Cell-wise cumulative density plots of GCaMP signal FWHM (purple) and AZ distances (blue). (**G**) Detail from (**F**); 6.5% of inter-AZ distances fall within 95% of GCaMP signal FWHM values. (**H**) Maximal projection of 100 s GCaMP video (grey) overlaid with registered confocal anti-BRP IHC (green). Green ROI: region shown in Figure 2 A. (**I**) Detail from (**H**): Left: 500 ms sequence (16-color LUT, contrast adjusted) of a single spontaneous SV fusion event attributed to a single AZ (white circle). Center: event assignment by signal strength within the ROIs. Right: Fluorescence traces from individual AZs in (**H**) for either spontaneous (orange) or AP-evoked (blue) SV release events. (**J**) Cell-wise mean±SEM (N = 15 animals) fluorescence traces of 670 spontaneous and 2849 AP-evoked events. (**K**) Single cell quantification of AZ-wise spontaneous events, plotted against corresponding AZ BRP-levels. Grey lines: fluorescence bin edges, r: Pearson's correlation coefficient (**L**) Same as (**K**) for AP-evoked activity. (**M**) Cell-wise activity levels (avg. events/AZ) plotted against normalized BRP fluorescence. Straight lines are linear fits on binned average data. See also Figure S1-2.

neighbor distance 0.679 ±0.003 µm, mean±SEM, N = 7 animals) and we wanted to determine the exact origin of each signal. We thus aligned higher resolution confocal BRP IHC images with GCaMP movies of live activity (**Fig. 1 H**) and collected temporal fluorescence profiles at equally sized regions of interest (ROIs) at all BRP-positive AZs. Although $Ca^{2+}$ dispersion could cause single GCaMP events to reach multiple ROIs (**Fig. 1 I**), signal intensity steeply decreased from the origin to the periphery, allowing signal assignment (highest peak) to the originating AZ (**Fig. 1 I**). In addition, a distance threshold was imposed such that no two AP-evoked events within 2.5 µm were allowed (only considering the higher-intensity event). This could cause a slight under-estimation of AP-evoked activity, but such situations are rare due to low per-AZ activity and this prevents wrongful assignment.

Spontaneous and AP-evoked neurotransmission events (100 s of imaging without stimulation, followed by 36 AP stimuli at 0.2 Hz) were assigned to single AZs (**Fig. 1 H-M** and **Fig. S1-1 A**). Simultaneous electrophysiological recordings confirmed that these events reported on synaptic transmission (**Fig. S1-1 C-E**). Fluorescence signals were similar for spontaneous- and AP-evoked release (**Fig. 1 J**) and non-saturating at 1.5 mM $[Ca^{2+}]_{ext.}$ (**Fig. S1-1 B**), confirming the quantal resolution of this assay (see methods and **Fig. S1-2**). Events were counted and assigned to each

bioRxiv preprint doi: https://doi.org/10.1101/2020.08.28.271742; this version posted August 30, 2020. The copyright holder for this preprint (which was not certified by peer review) is the author/funder, who has granted bioRxiv a license to display the preprint in perpetuity. It is made available under aCC-BY-ND 4.0 International license.

AZ, and only events exhibiting a peak in GCaMP fluorescence within 1 s of the AP were considered as AP-evoked (sufficient to capture asynchronous release and delayed GCaMP fluorescence responses). Based on this, release maps for either transmission mode were generated (**Fig. 2 A**). Because AZ size and function show high heterogeneity, responses at individual NMJs were scattered (**Fig. 1 K&L**). Another problem is the overall low per-AZ activity typical for NMJs, which achieves reliable responses by parallel action of many (~100-300) AZs. Longer acquisition times should provide a better estimate, but photobleaching and possible activity run-down complicate this. To provide a more reliable readout, responses were averaged across AZs based on their BRP fluorescence (**Fig. 1 M**). For this, AZs were sorted by fluorescence intensity and binned into 4 groups containing the same number of AZs. The mean number of events was plotted as a function of the mean AZ levels of BRP, revealing a positive linear dependence for both spontaneous and AP-evoked activity in individual examples (**Fig. 1K,L**) and most animals (**Fig. 1M**). These relationships were then averaged across several animals (12-19 per experiment; **Fig. 2**).

We observed a positive relation between single-AZ levels of BRP and both spontaneous and AP-evoked activity (**Fig. 2 B**), consistent with previous findings (64) and independent of recording sequence (i.e. spontaneous before AP-evoked activity or vice-versa; **Fig. S4 I-M**). Scaling of AP-evoked activity with BRP levels had been noted before (42, 43) and fits the observation that BRP colocalizes with the *Drosophila* VGCC subunit cacophony (Cac) (65), whose levels predict AP-evoked activity (66, 67). However, contrary to a reported negative correlation between BRP levels and spontaneous activity (investigated in-between AP-stimuli in mutant animals for the small GTPase Rab3; 42) we found a clear positive correlation (also noted in 64). The quantification in **Fig. 2 B** shows a cell-wise slope analysis of linear fits (tested against hypothetical zero slope) on

bioRxiv preprint doi: https://doi.org/10.1101/2020.08.28.271742; this version posted August 30, 2020. The copyright holder for this preprint (which was not certified by peer review) is the author/funder, who has granted bioRxiv a license to display the preprint in perpetuity. It is made available under aCC-BY-ND 4.0 International license.

average activity vs. BRP levels, demonstrating positive relations in both cases. BRP was used as AZ marker in all following analyses where we investigated how the levels of other, evolutionarily conserved presynaptic proteins related to both transmission modes (**Fig. 2 C-H**).

The AZ protein Unc13 (uncoordinated-13; 68), is essential for SVs to localize (dock) to the presynaptic plasma membrane and to gain fusion competence (prime) in invertebrates and mammals (reviewed in 69, 70, 12, 8, 71, 72). It substantially contributes to the generation of SV release sites in insects and mammals (64, 73, 74). Of the two major *Drosophila* isoforms, Unc13A dominates synaptic transmission at the NMJ, while Unc13B plays a minor role (75). Congruently, Unc13A AZ levels predicted AP-evoked and spontaneous transmission (**Fig. 2 C+D**), but no detectable scaling occurred with Unc13B levels (**Fig. 2 E+F**).

We next tested for a comparable influence on either release mode by syntaxin-1 (*Drosophila* isoform Syx-1A). As previously reported (64), AP-evoked activity scaled with Syx-1A AZ levels (**Fig. 2 G+H**). We here expanded this analysis to include spontaneous activity, also revealing a positive correlation with Syx-1A AZ levels.

Thus, our investigation of AZ activity in both NT release modes revealed overlapping relations among essential components of the SV release machinery. While the levels of BRP, Unc13A and Syx-1A all predicted activity levels in both transmission modes, no scaling was observed with regard to the Unc13B isoform.

bioRxiv preprint doi: https://doi.org/10.1101/2020.08.28.271742; this version posted August 30, 2020. The copyright holder for this preprint (which was not certified by peer review) is the author/funder, who has granted bioRxiv a license to display the preprint in perpetuity. It is made available under aCC-BY-ND 4.0 International license.

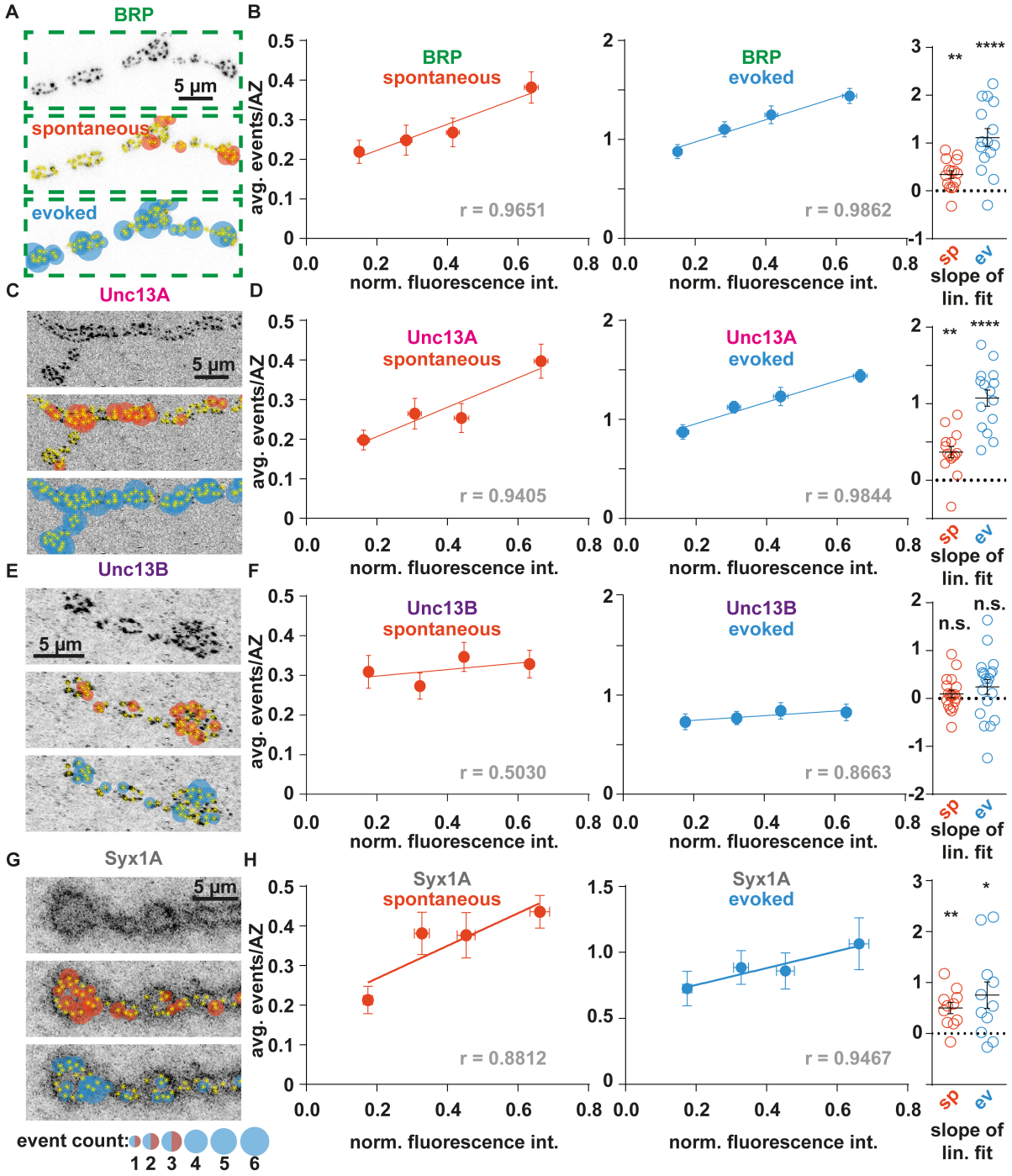


149

**Figure 2 Quantal single AZ $Ca^{2+}$-imaging shows influence of protein abundance on release modes.** (**A**) Top: 90° counter-clockwise rotated detail from **Figure 1 H**; Confocal image (inverted and contrast adjusted for illustration) of anti-BRP IHC. Middle: top image overlaid with BRP-positive AZs (yellow asterisks) and circle sizes indicating spontaneous activity levels. Bottom: top image overlaid with AP-evoked activity levels. (**B**) Left&Center: Binned normalized BRP fluorescence levels plotted against average number of spontaneous (orange) or evoked (blue) events at corresponding AZs. Right: Cell-wise slope quantification (N = 15 animals). (**C-H**) Same as (A&B), for Unc13A (N = 15 animals), Unc13B (N = 19 animals), and Syntaxin/Syx1A (N = 12 animals); yellow asterisks are AZ locations found in $\alpha$-BRP IHC. Statistical tests (Student's t-test) were performed against hypothetical 0 slope. Error bars indicate SEM. n.s. not significant; ** p<0.01; *** p<0.001; **** p<0.0001. Scale bars represent 5 µm. r values are Pearson's correlation coefficient. See also Figure S1-1.

bioRxiv preprint doi: https://doi.org/10.1101/2020.08.28.271742; this version posted August 30, 2020. The copyright holder for this preprint (which was not certified by peer review) is the author/funder, who has granted bioRxiv a license to display the preprint in perpetuity. It is made available under aCC-BY-ND 4.0 International license.

**Voltage-gated calcium channel block decreases spontaneous NT release**

APs evoke SV fusion by opening presynaptic VGCCs, causing local [$Ca^{2+}$] elevation, and Syt-1 activation (7, 9, 76, 77). As spontaneous transmission also depends on $[Ca^{2+}]_{int.}$ and Syt-1, and is diminished in Cac mutants (65, 44, 45), we wondered whether spontaneous NT release, like AP-evoked release, may be triggered by local [$Ca^{2+}$] elevations via VGCCs (48, 49). This could explain why we see spontaneous activity scaling with BRP (**Fig. 2 B**), whose levels correlate with VGCC abundance (78, 67, 66). We tested this by blocking $Ca^{2+}$ influx with $CdCl_2$ (Cadmium dichloride, which requires fairly high concentrations in this system 79) and optically assaying single AZ activity. We found that $CdCl_2$ slightly (statistically non-significantly) reduced the amplitudes of GCaMP signals (**Fig. 3 A**). However, a dramatic decrease in spontaneous event frequency (**Fig. 3 B**) was observed. Moreover, the strong dependence of spontaneous activity on the presynaptic BRP scaffold was weakened/lost (slope not statistically significantly different from 0) (**Fig. 3 C&D**).

We verified this in paired electrophysiological muscle membrane potential recordings before and after VGCC blockage. $CdCl_2$ inhibited all AP-evoked SV release (**Fig. 3 E)** and decreased spontaneous NT release frequency (though to a lesser extent than in GCaMP experiments). We also observed a decrease of mEJP (miniature excitatory junctional potential) amplitudes (**Fig. 3 G**), which might affect the detection of events. This effect may be of postsynaptic origin, as we saw no evidence of an altered membrane potential or resistance in these recordings (in 1.5 mM ext. $Ca^{2+}$; membrane potential: after ctrl: $V_{mem}$: -68.00±2.507 mV; after $CdCl_2$: -64.75±2.877 mV, $p = 0.2$; membrane resistance: after ctrl: $R_{mem}$: 12.75±1.485 MΩ; after $CdCl_2$: $R_{mem}$: 13.00±1.086 MΩ, $p = 0.8929$; N=8 animals in each case, paired parametric t-tests, mean±SEM).

bioRxiv preprint doi: https://doi.org/10.1101/2020.08.28.271742; this version posted August 30, 2020. The copyright holder for this preprint (which was not certified by peer review) is the author/funder, who has granted bioRxiv a license to display the preprint in perpetuity. It is made available under aCC-BY-ND 4.0 International license.

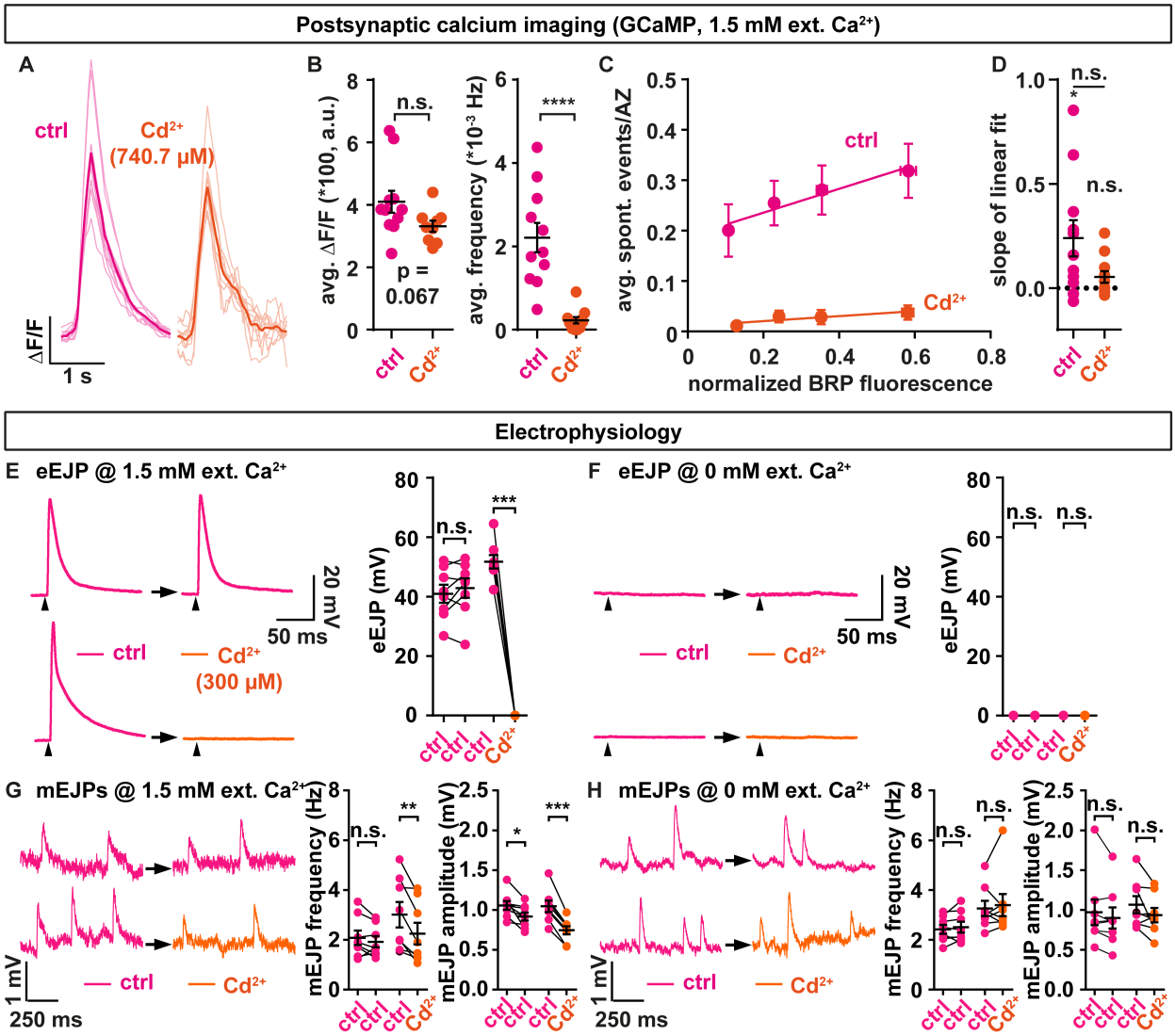


**Figure 3 Voltage-gated calcium channel block influences spontaneous neurotransmission.** (**A**) Single cell (faint) and animal-wise (solid) average spontaneous event GCaMP-fluorescence traces in either ctrl- (magenta) or $CdCl_2$-treated (740.7 µM; orange) animals. (**B**) Cell-wise quantification of GCaMP event amplitudes (left) (ctrl N = 11; $CdCl_2$ N = 9 animals (no spont. events in 2 animals treated with $CdCl_2$)) and frequency (right) (ctrl N = 11; $CdCl_2$ N = 11 animals). (**C**) Binned normalized BRP fluorescence values plotted against binned single AZ spontaneous activity levels in either control (magenta) or $Cd^{2+}$-treated (orange) conditions. (**D**) Cell-wise slope quantification in ctrl and $CdCl_2$ (N = 11 animals) conditions. Asterisks in (**D**) indicate significance deviation of 0 assessed by Student's t-test. (**E+F**) Left: Representative eEJP traces of ctrl cells (magenta) or cells treated with 300 µM $CdCl_2$ (orange) in either 1.5 **(E)** or 0 mM $[Ca^{2+}]_{ext.}$ with 2mM EGTA **(F)** in paired recordings. Right: Animal-wise quantification of eEJP amplitudes in ctrl → ctrl or ctrl → $CdCl_2$ in either 1.5 **(E)** or 0 mM $[Ca^{2+}]_{ext.}$ with 2 mM EGTA **(F)** (N = 8 animals in each of the 4 groups). Small arrows indicate time of stimulation (**G+H**) Left: Representative mEJP traces of ctrl cells (magenta) or cells treated with 300 µM $CdCl_2$ (orange) in either 1.5 **(G)** or 0 mM $[Ca^{2+}]_{ext.}$ with 2mM EGTA **(H)** in paired recordings. Right: Animal-wise quantification of mEJP amplitudes in ctrl → ctrl or ctrl → $CdCl_2$ in either 1.5 **(G)** or 0 mM $[Ca^{2+}]_{ext.}$ with 2 mM EGTA **(H)** (N = 8 animals in each of the 4 groups). Paired parametric t-tests were used for the analysis in **E-H**. Error bars indicate SEM. n.s. not significant; * $p<0.05$; ** $p<0.01$; *** $p<0.001$; **** $p<0.0001$.

bioRxiv preprint doi: https://doi.org/10.1101/2020.08.28.271742; this version posted August 30, 2020. The copyright holder for this preprint (which was not certified by peer review) is the author/funder, who has granted bioRxiv a license to display the preprint in perpetuity. It is made available under aCC-BY-ND 4.0 International license.

173 Notably, unlike in other systems, the spontaneous release rate at the *Drosophila* NMJ does not
174 depend on $[Ca^{2+}]_{ext.}$ (44, 33, 22, 51). Accordingly, reducing $[Ca^{2+}]_{ext.}$ to 0 mM (using 2 mM EGTA
175 to chelate all $Ca^{2+}$) did not diminish mEJP frequencies (**Fig. 3 H)**. The reason for this is unkown,
176 but could be independent of a change in $Ca^{2+}$ influx as a pathway mediated by a G-Protein coupled
177 $Ca^{2+}$-sensing receptor might control spontaneous transmission (80). Interestingly, in the absence
178 of $[Ca^{2+}]_{ext.}$, application of $Cd^{2+}$ did not affect mEJP frequency, arguing for a specific effect on
179 VGCC $Ca^{2+}$ influx (**Fig. 3 H)**. Thus, we see a sizable proportion of spontaneous events at
180 physiological conditions reduced upon VGCC block, consistent with some spontaneous activity
181 being triggered by $Ca^{2+}$ influx through stochastically gating/leaking VGCCs (as described in other
182 systems; 48–50).

183 **Neurotransmission in both release modes targets overlapping postsynaptic receptors**

184 Next, we wondered whether the same NT receptors detect both transmission modes (**Fig. 4 B**), or
185 whether they are dedicated to either transmission mode (**Fig. 4 A**), as implied by previous studies
186 (58, 42). We stimulated AP-evoked NT release in the presence of the use-dependent glutamate
187 receptor blocker Philanthotoxin (PhTx;) (59, 60), observing whether this affected spontaneous
188 transmission (**Fig. 4 C**). This would only occur if NT receptors promiscuously detected both
189 transmission modes, as the same receptors sensing spontaneous NT release would have been
190 blocked by PhTx due to AP-evoked NT release (**Fig. 4 A&B**).

191 We initially monitored baseline spontaneous transmission in electrophysiological current-clamp
192 experiments for 30 s before and after PhTx application, which expectedly reduced mEJP
193 amplitudes (**Fig. 4 D**) (60). In half of the animals, the efferent nerve was then stimulated with 100
194 APs (10 Hz, **Fig. 4 F**), a stimulation suitable to block glutamate receptors in the presence of PhTx
195 (**Fig. S3 D-F**). The other half of the animals received no AP stimulation (but saw a corresponding

bioRxiv preprint doi: https://doi.org/10.1101/2020.08.28.271742; this version posted August 30, 2020. The copyright holder for this preprint (which was not certified by peer review) is the author/funder, who has granted bioRxiv a license to display the preprint in perpetuity. It is made available under aCC-BY-ND 4.0 International license.

196 10 s wait) (**Fig. 4 E**). In both groups, mEJPs were then recorded for another 30 s. If spontaneous
197 and AP-evoked activity were exclusively sensed by distinct postsynaptic receptors, AP-stimulation
198 should not disrupt spontaneous transmission (**Fig. 4 A**). Contrasting this, a clear decrease of mEJP
199 frequency only occurred in the group receiving the AP stimulations (**Fig. 4 F**). The effect was
200 specific to the use dependent block of PhTx, as

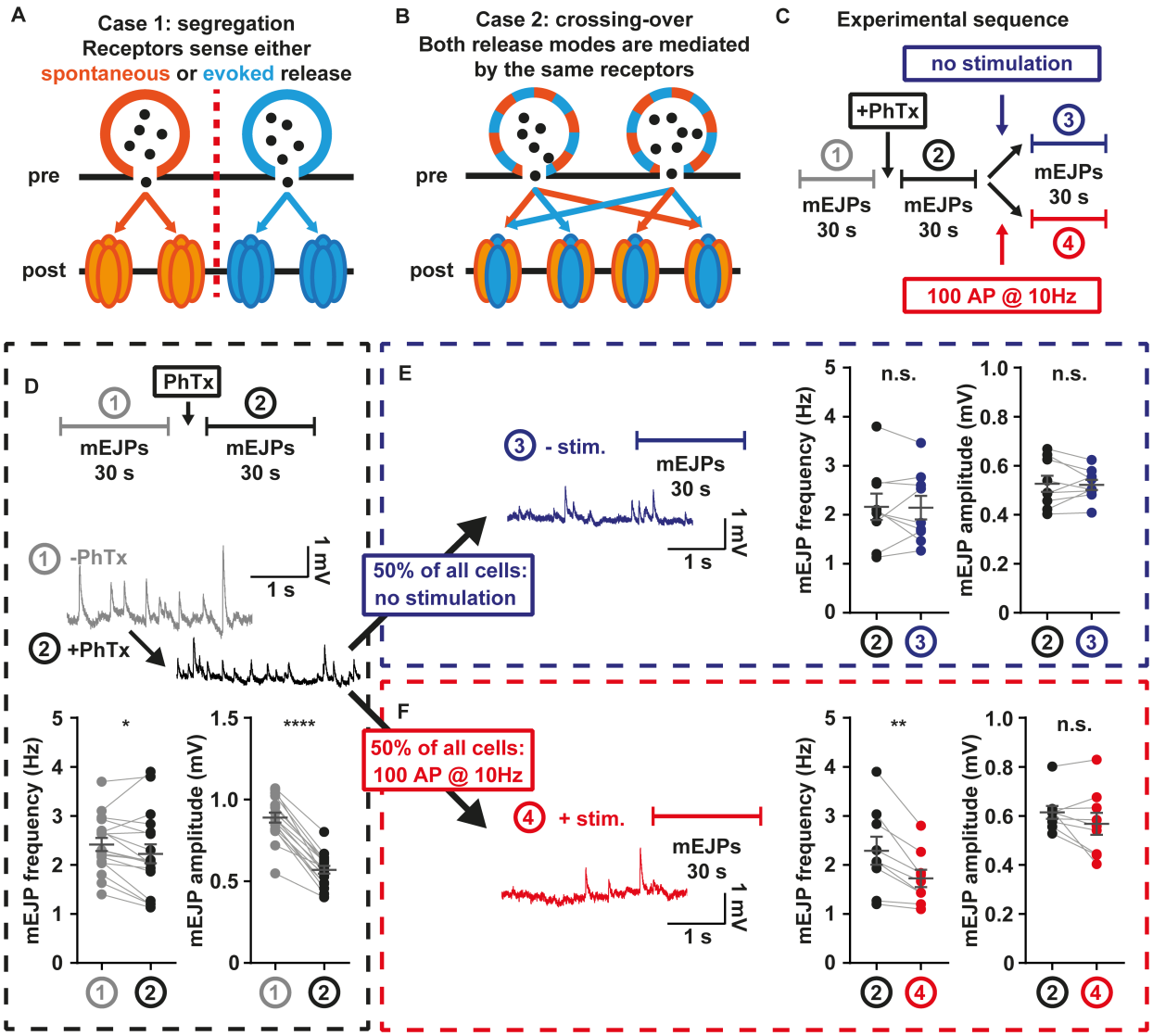


201

bioRxiv preprint doi: https://doi.org/10.1101/2020.08.28.271742; this version posted August 30, 2020. The copyright holder for this preprint (which was not certified by peer review) is the author/funder, who has granted bioRxiv a license to display the preprint in perpetuity. It is made available under aCC-BY-ND 4.0 International license.

**Figure 4 Postsynaptic receptors share sensitivity for both release modes.** (**A**) Illustration case 1: Spontaneous (orange) and AP-evoked (blue) transmission rely on distinct postsynaptic receptors. (**B**) Illustration case 2: Both release modes use the same postsynaptic receptors. (**C**) Experimental setup: After 30 s mEJP baseline recordings, larvae are treated with 4 µM PhTx, and another 30 s of mEJPs are recorded. Then, one half of animals (group 4, red) undergoes stimulation at 10 Hz over 10 s, the other half (group 3, blue) receives no stimulation. Another 30 s of mEJPs are recorded, yielding traces as shown in (D-F). (**D**) mEJP frequency and amplitude quantification before (grey) and after (black) PhTx application (N = 18 animals) (**E**) mEJP frequency and amplitude quantification after PhTx application and without stimulation (N = 9 animals) (**F**) mEJP frequency and amplitude quantification after PhTx application and with stimulation (N = 9 animals). Means are shown, error bars indicate SEM. n.s. not significant; * $p<0.05$; ** $p<0.01$; **** $p<0.0001$, paired t-test See also Figure S3.

stimulation alone had no effect (**Fig. S3 A-C**), arguing against SV pool depletion or receptor desensitization as underlying cause. Our data provide insight into PhTx function, because the effect was specific to mEJP frequency, without affecting amplitudes (**Fig. 4 F**). This is consistent with PhTx blocking receptors when they open upon exposure to glutamate leading to a diminished amplitude, while subsequent glutamate exposure elicits no detectable response in presence of PhTx. Regardless of the molecular details, our results show that receptor block induced by AP-evoked activity affects spontaneous neurotransmission, clearly indicating that both transmission modes activate the same receptors.

A previous study using a similar approach at the *Drosophila* NMJ concluded no effect of use-dependent NT receptor block across transmission modes (42). However, those experiments were compared across different groups of animals (which is less sensitive) and over far longer time (25 min vs. 10 s here) where compensatory, homeostatic mechanisms are known to take place with this treatment (60, 81, 82). Our finding does not preclude an additional coexistence of dedicated pathways, but it clearly demonstrates the shared use of NT receptors for both transmission modes during typical activity.

bioRxiv preprint doi: https://doi.org/10.1101/2020.08.28.271742; this version posted August 30, 2020. The copyright holder for this preprint (which was not certified by peer review) is the author/funder, who has granted bioRxiv a license to display the preprint in perpetuity. It is made available under aCC-BY-ND 4.0 International license.

**Spontaneous and AP-evoked transmission are correlated at single AZs and utilize the same SV pool**

Spontaneous and AP-evoked transmission were reported to originate from distinct AZs (41, 42). However, our observed common use of postsynaptic receptors and the similar dependence on the presynaptic release machinery partly implies the opposite. We thus investigated the correlation of AP-evoked and spontaneous NT release at single AZs (**Fig. 5**). In typical recordings, we sequentially measured spontaneous activity (100 s) before assessing AP-evoked activity from the same AZs (36 APs at 0.2 Hz) (**Fig. 5 A**). The release maps in **Fig. 5 A** illustrate the positions of NT release mapped during either episode and show a substantial number of AZs that exhibit mixed (spontaneous *and* AP-evoked) activity. Notably, the absolute numbers will depend heavily on the detectable events (i.e. acquisition time and stimulus number). When analyzing all individual events from AZs at a single NMJ (**Fig. 5 B**), we saw no obvious correlation ($r = 0.12$; $R^2 = 0.014$) between the number of spontaneous events per AZ and its probability to respond to APs (per-AZ release probability, $pAZ_r = \frac{number\ of\ evoked\ release\ events\ per\ AZ}{number\ of\ stimuli}$), agreeing with previous findings (41, 61). However, sampling across all AZs is problematic due to limited acquisition time and overall low per-AZ activity. To provide a better estimate, AZs were grouped by the number of spontaneous events and the mean $pAZ_r$s calculated. This revealed a considerably higher correlation in this animal ($r = 0.89$, $R^2 = 0.79$; **Fig. 5 B**). The effect became obvious when furthermore considering the mean $pAZ_r$ across many animals (N = 59 animals), which revealed a high correlation ($r = 0.98$, $R^2 = 0.97$; **Fig. 5 C**) between both release modes.

bioRxiv preprint doi: https://doi.org/10.1101/2020.08.28.271742; this version posted August 30, 2020. The copyright holder for this preprint (which was not certified by peer review) is the author/funder, who has granted bioRxiv a license to display the preprint in perpetuity. It is made available under aCC-BY-ND 4.0 International license.

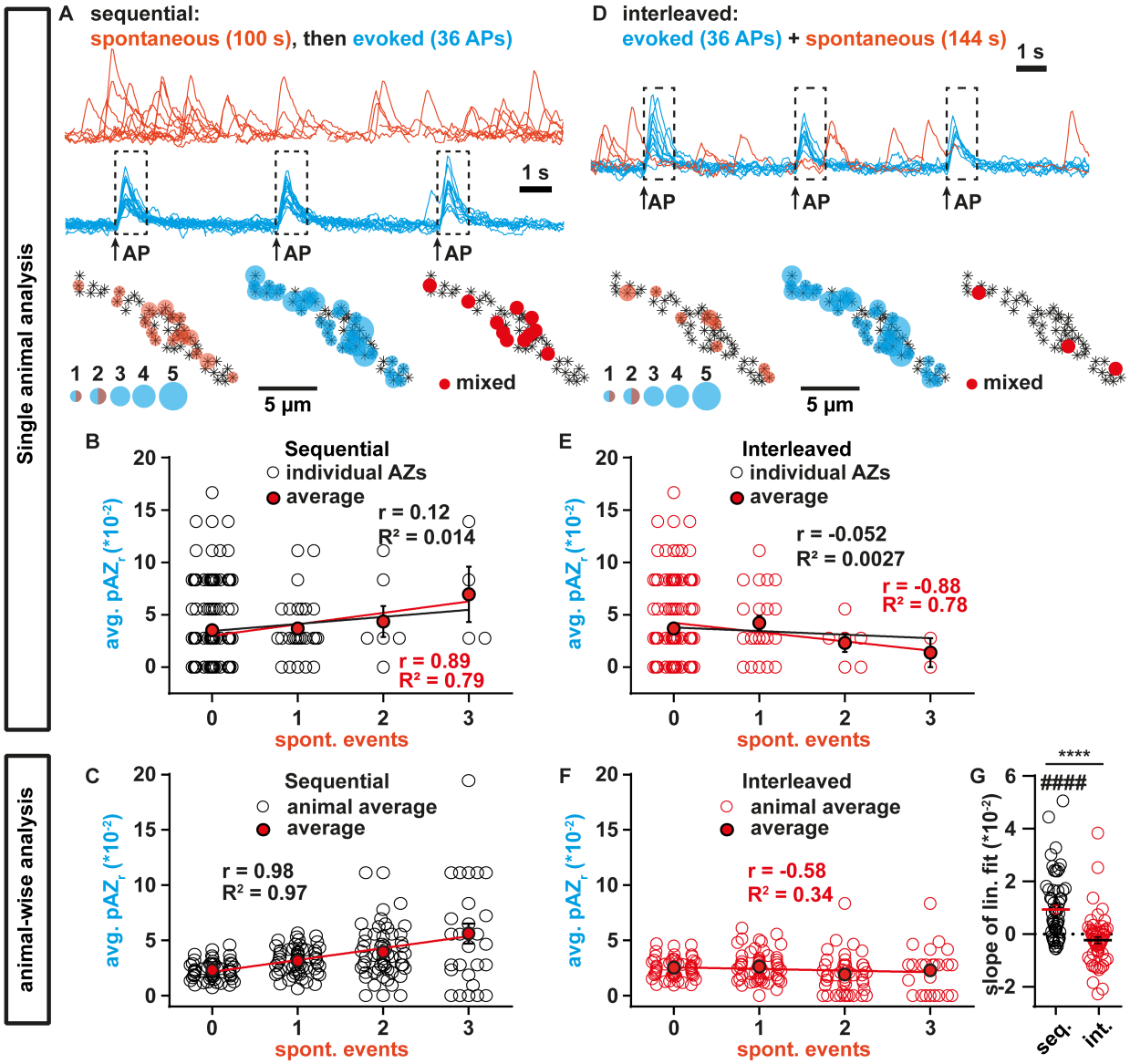


238

**Figure 5 Both release modes coexist at most AZs, are highly correlated and share an SV pool.** (**A**) "Sequential" experiment: spontaneous events (top, orange) are recorded for 100 s, then 36 APs are elicited at 0.2 Hz (bottom, blue). "Mixed" AZs showing both modes of release can be quantified (right). AZ-positions (asterisks) defined by anti-BRP IHC. Colored disk size corresponds to number of measured events. (**B**) Sequential measurement: Single NMJ AZ-wise spontaneous event number vs $pAZ_r$ (N = 148 AZs) Black circles represent single AZs; Black line: linear fit on all individual AZs; red line: linear fit through mean pAZ values (red dots). (**C**) "Sequential" experiment: Animal-wise (N = 59) spontaneous event count vs. average $pAZ_r$; black circles represent single NMJs, red dots represent means; red line: linear fit through means. (**D**) "Interleaved" experiment: 36 APs are given at 0.2 Hz (shaded blue), spontaneous events are measured in-between stimuli (shaded orange). "Mixed" AZs quantification (right). Asterisks signify AZ-positions defined by anti-BRP IHC. Colored disk size corresponds to number of detected events. (**E**) Interleaved measurement: Single NMJ AZ-wise spontaneous event count vs $pAZ_r$ (N = 148 AZs) Black circles represent single AZs; Black line: linear fit through all replicates; red line: linear fit through mean values (red dots). (**F**) "Interleaved" experiment: Animal-wise (N = 59) spontaneous event count vs. average $pAZ_r$; red circles represent single NMJs, red dots represent means; red line: linear fit through means. (**G**) Animal-wise (N = 59) quantification of linear fit slopes. Error bars indicate SEM. ****/#### $p<0.001$; Pound sign indicates t-test against hypothetical 0 slope. **C&F**: Only bins with >5 responding cells were taken into account in analysis. Refer to statistics table for details on mean values and testing. See also Figure S4.

bioRxiv preprint doi: https://doi.org/10.1101/2020.08.28.271742; this version posted August 30, 2020. The copyright holder for this preprint (which was not certified by peer review) is the author/funder, who has granted bioRxiv a license to display the preprint in perpetuity. It is made available under aCC-BY-ND 4.0 International license.

Thus, owing to a near-perfect correlation, the rate of spontaneous activity at individual AZs is a reliable predictor for their responsiveness to AP stimuli. Importantly, this is also the case when the experiment is performed using the inverse sequence (first measuring AP-evoked activity, then spontaneous activity; **Fig. S4 I&K**) which rules out effects of e.g. activity run-down and fluorescence bleaching.

Our finding does not exclude the existence of very specialized synapses (i.e. those engaging in only one transmission mode). In fact, some AZs only showed spontaneous activity during our recordings (**Fig. S4 A**), as reported previously (42, 41). However, this observation is not sufficient to conclude on dedication to specialized release modes, because whether an AZ will observably engage in AP-evoked transmission as well depends heavily on the acquisition time/number of APs given. Because this is limited, the low per-AZ activity at the NMJ poses a particular problem. Sampling more events in longer experiments could improve the estimate, but also adds uncertainty due to possible problems with photo-bleaching and rundown of synaptic activity. Methods to extrapolate how the system behaves for longer times are warranted and we quantitatively evaluated this in a survival analysis and exponential extrapolation. We tested two models, one in which all spontaneously active AZs eventually also engage in AP-evoked activity, and one where some AZ only exhibit spontaneous activity. While the latter model was favored (based on Akaike's information criterion; 83), most AZs were predicted to engage in both transmission modes: From all AZs active during the spontaneous recording episode, the vast majority (79 %) was predicted to additionally engage in AP-evoked transmission, while only 21% would exclusively transmit spontaneously (**Fig. S4 B&C**). This constitutes ~14% of all AZs responsive throughout the experiment, similar to an estimate of a classic study at the frog NMJ (84).

bioRxiv preprint doi: https://doi.org/10.1101/2020.08.28.271742; this version posted August 30, 2020. The copyright holder for this preprint (which was not certified by peer review) is the author/funder, who has granted bioRxiv a license to display the preprint in perpetuity. It is made available under aCC-BY-ND 4.0 International license.

Our findings of a near perfect positive correlation between transmission modes contradict a previous study reporting on a negative correlation (42). This incongruence may be explained by the Rab3 null-mutant background, and by an assessment of spontaneous activity in-between AP-stimuli used in that study (42). We wondered to what extent the recording paradigm influences the correlation between activity modes, which also allowed us to investigate overlap between SV pools utilized in both release modes (5, 85) by testing for cross-depletion. We quantified spontaneous activity in-between AP stimuli (**Fig. 5 D**) in the recordings previously used for analyzing AP-evoked single-AZ activity (**Fig. 5 A**). We found that the spontaneous event frequency was reduced while amplitudes were unaffected (frequencies – seq: 0.0037 Hz/AZ; int: 0.0018 Hz/AZ; N = 9 animals, p = 0.0003; amplitudes – seq: 786.8 a.u.; int: 845.5 a.u.; N = 9 animals, p = 0.13; paired parametric two-tailed t-test) and 39% fewer AZs were seen to engage in both transmission modes ("mixed", solid red circles in **Fig. 5 A&D**) (**Fig. S4 A,G,H**). This is consistent with AP-evoked activity reducing spontaneous transmission. Unlike for spontaneous events recorded in isolation, where AZ BRP levels predicted spontaneous activity (**Fig. 2 B**, **Fig. S4 D&F**), this correlation was lost/weakened (**Fig. S4 E&F**). Importantly, and consistent with the previous reports by 42, the correlation between spontaneous and AP-evoked transmission was now negative (**Fig. 5 E&F** and **Fig. S4 I-M**, where the experiment was performed in the reverse sequence and the correlation weakened). As the only difference between the two analyses is whether spontaneous activity is measured in isolation (**Fig. 5 A,B,C**) or in-between APs (**Fig. 5 D,E,F**), our results demonstrate a functional interdependence of the two transmission modes: AP-stimulation diminishes spontaneous activity and reverts the highly positive correlation between transmission modes. This indicates that APs cross-deplete an SV pool that also mediates spontaneous transmission and refills slowly at this sparse stimulation (0.2 Hz here, 0.1 Hz in 42). We conclude that both transmission

bioRxiv preprint doi: https://doi.org/10.1101/2020.08.28.271742; this version posted August 30, 2020. The copyright holder for this preprint (which was not certified by peer review) is the author/funder, who has granted bioRxiv a license to display the preprint in perpetuity. It is made available under aCC-BY-ND 4.0 International license.

modes utilize a common pool of SVs and that an individual assessment is necessary to unveil their molecular dependencies while the perturbance of one mode by the other proves their functional interdependence.

Our results suggest that previous claims regarding the specificity and functional independence of spontaneous neurotransmission may need revisiting in different experimental approaches. While some AZs appear specialized for spontaneous transmission, this only applies to a minority whereas the vast majority (~79%) also engages in AP-evoked transmission. It is tempting to speculate that these features relate to a developmental trajectory, with nascent AZs containing the essential machinery required to engage in spontaneous NT release needed for maturation (5, 4), yet lacking some of the more specialized machinery to tune activity to APs (86, 67, 87). The ability to observe such AZs might greatly depend on the maturity of the model system, possibly explaining some of the differences in *Drosophila* larvae and cultured neurons. While this remains speculation, we show that both transmission modes coexist at AZs and are correlated. They utilize the same presynaptic molecular machinery (SV priming and fusion proteins, VGCCs, likely organized by AZ scaffolding proteins), draw on the same SV pool, and activate the same NT receptors. One can easily imagine that this interdependence serves important biological functions, for instance in the regulation of synaptic strength. Indeed, spontaneous activity is sufficient to homeostatically regulate AP-evoked transmission (81). This appears possible because spontaneous activity constitutes a continuous, stimulus-independent, and scalable representation of AP-evoked signal strength at the same AZ.

bioRxiv preprint doi: https://doi.org/10.1101/2020.08.28.271742; this version posted August 30, 2020. The copyright holder for this preprint (which was not certified by peer review) is the author/funder, who has granted bioRxiv a license to display the preprint in perpetuity. It is made available under aCC-BY-ND 4.0 International license.

# Materials & Methods

## Resources Table

| REAGENT or RESOURCE | SOURCE | IDENTIFIER |
|---|---|---|
| Antibodies | | |
| primary: mouse anti Syntaxin-1A | Developmental Studies Hybridoma Bank | Cat# 8c3, RRID:AB_528484 |
| primary: guinea pig anti Unc13A | Böhme et al., 2016 | n/a |
| primary: rabbit anti Unc13B | Böhme et al., 2016 | n/a |
| primary: mouse anti $BRP^{c\text{-}term}$ | Developmental Studies Hybridoma Bank | Cat# nc82, RRID:AB_2314866 |
| primary: rabbit anti $BRP^{last200}$ | Ullrich et al., 2015 | n/a |
| secondary: donkey anti guinea pig DyLight 405 | Jackson ImmunoResearch | Cat# 106-475-003, RRID: AB_2337432 |
| secondary: goat anti mouse Cy3 | Jackson ImmunoResearch | Cat# 115-165-146, RRID: AB_2338690 |
| secondary: goat anti rabbit Cy3 | Jackson ImmunoResearch | Cat# 111-165-144, RRID: AB_2338006 |
| Experimental Models: Organisms/Strains | | |
| *D. melanogaster*: Wild type: *w1118* | own lab stock | n/a |
| *D. melanogaster: Mhc-myr-gcamp5g/III* | Reddy-Alla et al., 2017 | n/a |
| Software and Algorithms | | |
| MATLAB | Mathworks Inc. | R2016b |
| ImageJ | NIH | v1.48q/v1.52i |
| MicroManager | https://micro-manager.org | v1.4.2 |
| Custom MATLAB code | this paper/Reddy-Alla et al., 2017 | n/a |
| Custom ImageJ code | this paper/Reddy-Alla et al., 2017 | n/a |

bioRxiv preprint doi: https://doi.org/10.1101/2020.08.28.271742; this version posted August 30, 2020. The copyright holder for this preprint (which was not certified by peer review) is the author/funder, who has granted bioRxiv a license to display the preprint in perpetuity. It is made available under aCC-BY-ND 4.0 International license.

| | | |
|---|---|---|
| LAS AF Lite | Leica Microsystems | v2.6.3 |
| LAS X | Leica Microsystems | n/a |
| Clampfit | Molecular Devices | v10.5/10.6.2.2 |
| Graphpad Prism | GraphPad Software | v6.01 |
| Pharmacological agents | | |
| Philanthotoxin-433 | Sigma Aldrich | Cat# P207 |
| Cadmium dichloride | Sigma Aldrich | Cat# 202908 |
| EGTA tetrasodium salt | Sigma Aldrich | Cat# E8145 |
| Other | | |
| Leica SP8 confocal microscope | Leica Microsystems | n/a |

306

307 **Animal rearing and preparation**

308 Experiments making use of genetically modified invertebrate animals have been registered with
309 and approved by the respective authorities (Landesamt für Gesundheit und Soziales LaGeSo,
310 Berlin), and were performed in accordance with German laws and regulations on biosafety.
311 Animals were bred and maintained at standard laboratory conditions (88) on semi-defined fly
312 medium (Bloomington recipe). Male and female flies were used for all experiments. Wild type
313 *w1118* flies were used for the experiments shown in **Fig.3 E-H** and **Fig. 4**. The following fly strain
314 was used for all other experiments: *Mhc-myrGCaMP5G/+;* (64). Third instar larvae were dissected
315 as described in 89 in standard $Ca^{2+}$-free, hemolymph-like solution HL-3 (composition in mM: 70
316 NaCl, 5 KCl, 20 $MgCl_2$, 10 $NaHCO_3$, 5 Trehalose, 115 Sucrose, 5 HEPES; 90; low $Mg^{2+}$-solution
317 used for PhTx-electrophysiology experiments contained 10 mM $MgCl_2$), adjusted to pH=7.2.
318 Dissection was performed using fine insect pins on Sylgard-184 (Dow Corning, Midland MI,
319 USA), by opening the dorsal body wall from posterior to anterior, removing all internal organs,

bioRxiv preprint doi: https://doi.org/10.1101/2020.08.28.271742; this version posted August 30, 2020. The copyright holder for this preprint (which was not certified by peer review) is the author/funder, who has granted bioRxiv a license to display the preprint in perpetuity. It is made available under aCC-BY-ND 4.0 International license.

and severing the motoneurons from the CNS without damaging the underlying body wall muscles, then removing the brain. For experimentation, the dissected larvae were then transferred to recording chambers on the respective recording setups, as detailed in the sections explaining electrophysiology and live calcium imaging.

**Electrophysiology**

All electrophysiological experiments were performed at room temperature using sharp glass electrodes (borosilicate glass with filament, 0.86x1.5x80 nm, Science products, Hofheim, Germany) pulled with a Flaming Brown Model P-97 pipette puller (Sutter Instruments, CA, USA). Stimulating suction electrodes were pulled on a DMZ-Universal Puller (Zeitz-Instruments GmbH, Germany) and fire polished using a CPM-2 microforge (ALA Scientific, NY, USA). Recordings were performed in current clamp mode at muscle 6 (PhTx experiments) / muscle 4 ($Cd^{2+}$ experiments) in segments A2/A3 as previously described (91) using an Axon Digidata 1550A digitizer, Axoclamp 900A amplifier with HS-9A x0.1 headstage (Molecular Devices, CA, USA) and on a BX51WI Olympus microscope with a 40X LUMPlanFL/IR water immersion objective. Sharp intracellular recording electrodes with a resistance of 20-35 MΩ were made and back-filled with 3 M KCl. Only cells with membrane potentials below -60 mV (PhTx experiments) / -40 mV ($Cd^{2+}$ experiments) and membrane resistances greater than 4 MΩ were considered. Recordings were acquired using Clampex software (v10.5) and sampled at 10-50 kHz, filtering with a 5 kHz low-pass filter. Analysis for all electrophysiological datasets was performed with Clampfit (v10.5/10.6.2.2) and Graphpad Prism 6 software. mEJPs were further filtered with a 500 Hz Gaussian low-pass filter. A single mEJP template was generated for each cell and used to identify individual mEJPs, and to calculate the mean mEJP amplitude and frequency per cell.

bioRxiv preprint doi: https://doi.org/10.1101/2020.08.28.271742; this version posted August 30, 2020. The copyright holder for this preprint (which was not certified by peer review) is the author/funder, who has granted bioRxiv a license to display the preprint in perpetuity. It is made available under aCC-BY-ND 4.0 International license.

**Current clamp experiments to determine VGCC role in spontaneous SV release**

Current clamp recordings using $CdCl_2$ in order to block VGCCs were performed at room temperature from muscle 4 of abdominal segments A2-A4 (**Fig. 3**) using 2 ml standard HL3 medium containing either 1.5 mM $CaCl_2$ **(Fig. 3 E&G)** or 0 mM $CaCl_2$ together with 2 mM of the $Ca^{2+}$ chelator EGTA-tetrasodium salt (Sigma, Germany, E8145) to buffer residual $Ca^{2+}$ traces **(Fig. 3 F&H)**. Recordings shown in **Fig. 3 E-H** were obtained in the presence of 300 µM $CdCl_2$ (orange) or the equivalent volume of $dH_2O$ as control (magenta) (see pharmacology section) in a strictly paired fashion. In detail, starting with a $CdCl_2$-free extracellular medium ("ctrl") a single AP was evoked in motoneurons (8 V, 300 µs pulse) using an ISO-STIM 01D stimulator (NPI Electronic, Germany) followed by a 30 s resting period. Sequentially, spontaneous mEJPs were recorded for 30 s followed by an immediate exchange of 1 ml bath solution (2 ml total bath volume) by 600 µM $CdCl_2$-HL3 ("$Cd^{2+}$") or $dH_2O$-HL3 ("ctrl") within a resting period of 2 min. Afterwards, another single AP was evoked followed by 30 s rest and recording of 30 s spontaneous activity. eEJP amplitudes were determined by quantifying the maximal voltage deflection following an AP (values in the standard noise range were considered as zero).

**Current clamp experiments to determine receptor sensitivity to different SV release modes**

For current clamp experiments using PhTx to determine postsynaptic receptor field sensitivity to both release modes (**Fig. 4**), the Sylgard block and completed larval preparation was placed in the recording chamber which was filled with 2 ml HL3 (0.4 mM $CaCl_2$, 10 mM $MgCl_2$). eEJPs were recorded by stimulating the appropriate nerve at 10 Hz, 100 times (8 V, 300 µs pulse) using an ISO-STIM 01D stimulator (NPI Electronic, Germany).

Spontaneous mEJPs for analysis shown in **Fig. 4 (D-F)** and **Fig. S3 (A-C)** were recorded for 30 seconds. 1 ml of solution was then removed from the bath without disturbing the preparation or

bioRxiv preprint doi: https://doi.org/10.1101/2020.08.28.271742; this version posted August 30, 2020. The copyright holder for this preprint (which was not certified by peer review) is the author/funder, who has granted bioRxiv a license to display the preprint in perpetuity. It is made available under aCC-BY-ND 4.0 International license.

electrodes and 1 ml of HL3 added containing PhTx-433 (Sigma-Aldrich, MO, USA), mixing gently with the pipette to a final bath concentration of 4 µM PhTx. Spontaneous mEJPs were recorded immediately, again for 30 seconds. Stimulation was performed at 10 Hz for 10 seconds to measure eEJPs or, in the case of control recordings, 10 seconds passed without stimulation. Finally, mEJPs were recorded for 30 seconds. Recordings shown in **Fig. S3 (A-C)** were performed as above, using HL3 lacking PhTx-433, as the exchange solution.

**Pharmacology**

Philanthotoxin (PhTx-433) used for experiments in **Fig. 4** was obtained from Sigma Aldrich (subsidiary of Merck KGaA, Darmstadt, Germany) and diluted to a stock concentration of 4 mM in $dH_2O$. In experiments, it was used at a concentration of 4 µM in HL-3 by applying it directly to the bath (see electrophysiology method section). Cadmium dichloride ($CdCl_2$) used for experiments shown in **Fig. 3** was obtained from Sigma Aldrich, diluted to a stock concentration of 300 mM in $dH_2O$, and used at a final concentration of 1:1000/300 µM in HL-3 for electrophysiological experiments shown in **Fig. 3 E-H**. For GCaMP experiments shown in **Fig. 3 A-D**, it was diluted to a stock concentration of 10 mM and used at a final concentration of 740.7 µM in HL-3 (1.12 mL 10 mM $CdCl_2/dH_2O$ stock in 14 mL HL-3 and a corresponding amount of 1.12 mL $dH_2O$ in controls, diluting the HL-3 components to (in mM): 64.8 NaCl, 4.63 KCl, 18.52 $MgCl_2$, 9.26 $NaHCO_3$, 4.63 Trehalose, 106.48 Sucrose, 4.63 HEPES); imaging began after 2 minutes of incubation time. Control experiments were performed using the same amounts of the respective solvent ($CdCl_2$: $dH_2O$, PhTx: $dH_2O$).

bioRxiv preprint doi: https://doi.org/10.1101/2020.08.28.271742; this version posted August 30, 2020. The copyright holder for this preprint (which was not certified by peer review) is the author/funder, who has granted bioRxiv a license to display the preprint in perpetuity. It is made available under aCC-BY-ND 4.0 International license.

**Live Calcium-Imaging**

GCaMP live imaging experiments were conducted in 2 mL HL-3 containing 1.5 mM $CaCl_2$ (except for $Ca^{2+}$-titration in **Fig. S1-1 B**: 0.4, 0.75, 1.5, 3, 6, 12 mM) on an Olympus BX51WI epifluorescence microscope, using a water immersion LUMFL 60x 1.10 w objective. A Lambda DG-4 (Sutter Instrument Company, Novato CA, USA) white light source was used to illuminate the samples through a GFP excitation/emission filter set. For experiments in Fig. 2 A-D, Fig. S4 D-M, and Fig. S1-1 B, a newer light source of the same model was used in combination with an Olympus ND25 neutral density filter. Images were acquired in camera-native 16-bit grayscale using an Orca Flash v4 sCMOS camera (Hamamatsu Photonics, Hamamatsu, Japan) under constant illumination with an exposure of 50 ms per frame, resulting in an effective imaging frame rate of 20 Hz. For all GCaMP analysis, spontaneous events were recorded from 1b NMJs in muscle 4, abdominal segments 2-4, for 100 s (120 s in the case of $Cd^{2+}$ experiments shown in **Fig. 3**). For experiments involving the imaging of AP-induced ('evoked') events, the efferent motoneuronal axon bundle innervating the same muscle was sucked into a polished glass capillary containing bath HL-3. The glass capillary was held in place by a patch electrode holder (npi electronic, Tamm, Germany), and contained a chlorided silver wire electrode, which connected to a pipette holder (PPH-1P-BNC, npi electronic, Tamm, Germany). After recording of spontaneous events, 36 single stimuli were applied as a square depolarization pulse of 300 µs at 7 V, 0.2 Hz for 180 s using a connected S48 stimulator (Grass Technologies, now part of Natus Medical Inc., Pleasanton, CA, USA), except for analysis shown in **Fig. S4 I-M**, where the experimental sequence was reversed. Imaging start/end was controlled by µManager software (version 1.4.20, https://micro-manager.org), and stimulation was administered through software (Clampex 10.5.0.9, Molecular Devices, San Jose, CA, USA) controlling a DA/AD converter (DigiData 1440A, Molecular

bioRxiv preprint doi: https://doi.org/10.1101/2020.08.28.271742; this version posted August 30, 2020. The copyright holder for this preprint (which was not certified by peer review) is the author/funder, who has granted bioRxiv a license to display the preprint in perpetuity. It is made available under aCC-BY-ND 4.0 International license.

Devices, San Jose, CA, USA). All videos acquired in 16-bit were then converted to 8-bit using ImageJ (version 1.48q). See section Image processing and analysis for further procedures and details.

**Immunohistochemistry**

After live imaging experiments, larval tissue was fixated for 7 min at -20°C using fresh Methanol for experiments involving IHC stainings against Unc13A, or for 10 min at RT using fresh 4% PFA in 0.1 mM PBS for all other experiments (i.e. involving IHC for BRP, Syx1A, Unc13B). Fixated samples (max. 8 per 1.5 mL sample cup) were then stored in 1 mL 1xPBS until all samples had been collected, but 6 hours at most. Then, off-target epitope blocking was performed in 1xPBS containing 0.05% Triton-X100 (PBS-T) and 5% normal goat serum (NGS) (total volume: 1000 µL) for 45 min on a wheel at RT, 17 rpm. Immediately after, the mix was replaced by an identical mixture and the respective first antibody was added at the following concentrations: mouse Syntaxin-1A 8C3 (1:40, Developmental Studies Hybridoma Bank, University of Iowa, Iowa City, IA, USA), guinea pig Unc13A (1:500) (75), rabbit Unc13B (1:1000) (75), mouse $BRP^{C\text{-}term}$ (1:1000, Developmental Studies Hybridoma Bank, University of Iowa, Iowa City, IA, USA), rabbit $BRP^{last200}$ (1:1000) (92). Samples were incubated with the primary antibody overnight (15-16 h) at 4°C on a sample wheel. Afterwards, samples were washed four times in PBS-T for 30 min at RT. Secondary antibodies were applied (4 h, RT) in PBS-T containing 5% NGS at the following concentrations: donkey anti guinea pig DyLight 405 (1:500, Jackson ImmunoResearch, West Grove, PA, USA), goat anti mouse Cy3 (1:500, Jackson ImmunoResearch), goat anti rabbit Cy3 (1:500, Jackson ImmunoResearch, West Grove, PA, USA). After this, they were washed with PBS for 30 min and finally mounted on 26x76 mm glass slides (Paul Marienfeld GmbH, Lauda-Königshofen, Germany) in VectaShield (Vector Laboratories, subsidiary of Maravai Life

bioRxiv preprint doi: https://doi.org/10.1101/2020.08.28.271742; this version posted August 30, 2020. The copyright holder for this preprint (which was not certified by peer review) is the author/funder, who has granted bioRxiv a license to display the preprint in perpetuity. It is made available under aCC-BY-ND 4.0 International license.

Sciences, San Diego, CA, USA) under 18x18 mm cover glass slides (Carl Roth GmbH, Karlsruhe, Germany) using clear nail polish to seal off the sides of the cover glass slide. The samples were then stored at 4°C and imaged within a week as described in the confocal microscopy and image processing section.

**Confocal microscopy and image processing**

Confocal imaging of immunohistochemically stained samples was performed on a Leica SP8 confocal quadruple solid-state laser scanning system (excitation wavelengths: 405, 488, 552, 635 nm), and operating on LAS X software (Leica Microsystems, Wetzlar, Germany) with a 63x 1.4 NA oil immersion objective at room temperature. Pixel edge length was 100 nm at a zoom factor of 1.8 and a z-step size of 0.5 µm for all datasets. Care was taken to choose fluorophores with non-overlapping excitation/emission spectra (see immunohistochemistry section), and confocal GCaMP images were always acquired without additional IHC at 488 nm excitation. Single z-stack images from all channels were exported from the proprietary .lif-format into TIF images using LAS AF Lite software (version 2.6.3, Leica Microsystems, Wetzlar, Germany) and converted to 8-bit grayscale maximal projections using custom ImageJ/Fiji software (version 1.52i, available upon request).

**Image processing and analysis**

**Stabilization of live-imaging videos**

As further analysis of GCaMP live-imaging videos was highly reliant on a stable position of the NMJ over time, all 2D-translational movement (in x,y-direction) of the muscle during the recording had to be corrected for. This was done as shown in 64, and is described in the following. Converting videos of mhc-myr-GCaMP5G from 16-bit to 8-bit grayscale was done in ImageJ.

bioRxiv preprint doi: https://doi.org/10.1101/2020.08.28.271742; this version posted August 30, 2020. The copyright holder for this preprint (which was not certified by peer review) is the author/funder, who has granted bioRxiv a license to display the preprint in perpetuity. It is made available under aCC-BY-ND 4.0 International license.

After conversion from 16-bit to 8-bit, the 8-bit multipage .TIF-video file ('stack') was loaded into MATLAB and a subregion of the first frame, containing the whole GCaMP-positive 1b NMJ, was chosen as a reference for the registration process using the MATLAB function *getrect*. Using the MATLAB function *normxcorr2*, every subsequent frame was then 2D-translated by a simple *x,y*-shift until the highest cross-correlation between pixel values of the current frame and the first frame was achieved. This procedure was repeated for all pairs of the first frame and succeeding frames. For this procedure, all images were Gaussian filtered (MATLAB function *imgaussfilt*) with a sigma value of 5 for noise reduction.

**Alignment of confocal images to live-imaging videos**

Next, we compensated for fixative-induced anisotropic deformation, orientation and size changes in confocal images by registering them to GCaMP-videos in ImageJ using the plugin "TurboReg" (Biomedical Imaging Group, EPFL, Switzerland; 93). An affine transformation that used three reference points in each image applied *x,y*-translation, rotation, and *x,y*-shearing where necessary to get the optimal overlay between GCaMP-signal in confocal and live-imaging. In rare instances, a bilinear transform using 4 reference points was necessary to achieve sufficient overlay between confocal image and GCaMP video. The necessary transformation found for the confocal GCaMP image was then applied identically to all other channels.

**Quantification of single AZ protein- and activity-levels**

In order to quantify protein and activity levels on the level of single AZs, we first defined ROIs in the confocal BRP channel by applying the ImageJ function *find maxima* using threshold values between 10 and 20. Circular ROIs with a diameter of 650 nm were centrally overlaid at all *x,y*-positions found with this procedure. The integrated density (sum of intensities of all pixels whose sub-pixel center lay within the borders of the circle) in all ROIs was then saved for each confocal

bioRxiv preprint doi: https://doi.org/10.1101/2020.08.28.271742; this version posted August 30, 2020. The copyright holder for this preprint (which was not certified by peer review) is the author/funder, who has granted bioRxiv a license to display the preprint in perpetuity. It is made available under aCC-BY-ND 4.0 International license.

frame and live-imaging frame in .xls-format for later analysis in MATLAB. Additionally, a file with all corresponding *x,y*-coordinates of all ROIs was saved as a text file. Further, to correct for unspecific background fluorescence decay due to photobleaching, we shifted all ROIs to a region without GCaMP fluorescence and generated another .xls-file containing the fluorescence values in these ROIs over time. These values were later subtracted from the corresponding fluorescence signal in the original ROIs.

We then loaded these files into MATLAB for further analysis. First, we determined all inter-AZ distances (all distances between every possible pair of AZs) using the squared Euclidean distance as shown in equation (1).

$$(1)\ dist(ROIa, ROIb) = sz_{px} * \sqrt{(d_x(ROIa, ROIb))^2 + (d_y(ROIa, ROIb))^2}$$

In equation (1), $ROIa$ and $ROIb$ are any of the determined ROIs, $sz_{px}$ is the physical pixel edge length of $0.108\overline{33}$ µm, and $d_x$ and $d_y$ are the vertical or horizontal pixel shift values in *x* or *y*, respectively, between both compared ROIs. This resulted in a diagonally symmetrical matrix of all possible inter-AZ distances. This distance was then used to exclude detecting another event within 2.5 µm (evoked activity measurements) or 1000 µm (spontaneous activity measurements) around one event in the same frame. We added another layer of security to exclude the detection of the same event twice by only considering the ROI with the highest amplitude within the given distance threshold and a single frame (each frame representing 20 ms of recording time).

Single AZ protein levels were normalized to a range between 0 and 1 as shown in equation (2). This procedure accounted for inter-experimental variability and allowed the direct comparison of different proteins.

bioRxiv preprint doi: https://doi.org/10.1101/2020.08.28.271742; this version posted August 30, 2020. The copyright holder for this preprint (which was not certified by peer review) is the author/funder, who has granted bioRxiv a license to display the preprint in perpetuity. It is made available under aCC-BY-ND 4.0 International license.

(2) $Signal_{norm} = \frac{Signal - \min(Signal)}{\max(Signal) - \min(Signal)}$

The GCaMP fluorescence over time of each ROI was corrected for photobleaching as described before, by subtracting the fluorescence measured in the corresponding background ROI. We then performed a linear fit on each single fluorescence trace over time (separately for spontaneous and AP-evoked activity recordings), yielding two parameters reflecting its slope and y-intercept (MATLAB function *polyfit*). Using these parameters (slope $s$ and y-intercept $int$), we performed a baseline correction for each time step $t$ and each $ROI$ as shown in equation (3).

(3) $Fluo_{GCaMP,corr}(t, ROI) = Fluo_{GCaMP}(t, ROI) - (t * s(ROI) + int(ROI))$

A custom procedure was then used to detect single peaks in the resulting fluorescence traces. All fluorescence traces were filtered by a 1D-filter using the MATLAB function *filter* (filter width: 5 frames). We then manually evaluated all instances in the fluorescence trace where the mean of the unfiltered signal over three consecutive frames exceeded a threshold of four times the SD of the filtered signal. As stated above, a circular distance threshold of 2.5 µm (AP-evoked activity measurements) or 1000 µm (spontaneous activity measurements) around each event was enforced to avoid unspecific detection of close by events in a single frame. When analyzing AP-evoked activity measurements, we only considered events that were detected within 1 s of the stimulus.

In order to generate activity maps as those shown in Fig. 2 (panels A,C,E, and G), we counted the number of detected events in each ROI and overlaid an inverted and contrast-adjusted IHC image of the respective protein at the NMJ with circles of corresponding sizes. The average signals shown in Fig. 1 J were generated by averaging all detected events in each cell, and then averaging over all cell means.

bioRxiv preprint doi: https://doi.org/10.1101/2020.08.28.271742; this version posted August 30, 2020. The copyright holder for this preprint (which was not certified by peer review) is the author/funder, who has granted bioRxiv a license to display the preprint in perpetuity. It is made available under aCC-BY-ND 4.0 International license.

The correlation of normalized protein levels and average activity levels per AZ shown in Fig. 2 (panels B,D,F,and H) was done as follows. First, we counted the number of events for each AZ as done for the activity maps. We then sorted the list of per-AZ event numbers and the list of AZ intensities by ascending intensity. Then, the lists were binned into four bins so that each bin contained the same amount of AZs. In each bin, we then averaged the fluorescence of all AZs and the corresponding number of events, yielding the number of events per AZ. For the graphs shown in **Fig. S4 (panels D, E & G)** we further divided the spontaneous events per AZ by the recording time (100 s) and the evoked events per AZ by the number of stimuli (36 APs).

**Spontaneous event detection between evoked events**

Besides the "sequential" way of analyzing spontaneous activity measurements and then evoked activity measurements as described above, we also quantified spontaneous events that happened between stimuli ("interleaved") as shown in Fig. 5 (E&F) and **Fig. S4 (E&L)**. For this, we altered the procedure described above by one detail. While everything else happened as in our conventional approach to measure spontaneous activity, we suppressed the detection of evoked events and instead quantified SV release between stimuli by creating an exclusion list. This list included all time points 1000 ms after the stimulus, within which no fluorescence peaks would be considered as a signal. When analyzing spontaneous event frequency (**Fig. S4 D,E & G**), to account for the differing time over which spontaneous events were recorded (100 s in sequential analysis vs. 144 s in interleaved analysis), we divided activity levels by the respective recording time.

**Survival analysis**

A survival analysis quantifies the amount of "surviving" samples (in this case exclusively spontaneously active AZs) in face of an event that "kills" those samples (in this case trying to

bioRxiv preprint doi: https://doi.org/10.1101/2020.08.28.271742; this version posted August 30, 2020. The copyright holder for this preprint (which was not certified by peer review) is the author/funder, who has granted bioRxiv a license to display the preprint in perpetuity. It is made available under aCC-BY-ND 4.0 International license.

evoke release by a stimulus), i.e. switches them from one state to another over the course of the treatment. To analyze how many spontaneously active ROIs would "survive", or maintain their exclusively spontaneous state by not showing any AP-evoked activity in the AP-evoked activity measurement (**Fig. S4 B**), we proceeded as follows. We loaded the results from the analysis of spontaneous and AP-evoked activity measurements (described above) containing all activity time points and AZ identities of spontaneous or evoked events into MATLAB. We then first found the number and identity of all AZs showing spontaneous activity. We created a data vector containing as many data points as there were frames in the AP-evoked activity recording (3600 over 180 s) and filled all positions with the number of AZs showing spontaneous activity we had found. Then, we found all time points of AP-evoked events in these AZs and subtracted 1 from the previously created vector at the time points of the evoked event to the end of the vector, resulting in a decreasing amount of exclusively spontaneously active AZs over the time of the AP-evoked activity measurement. For each cell, we then set the initial amount of exclusively spontaneously active AZs in that cell to 1 (100 %). Two models describing the mono-exponential survival decay were compared using Akaike's information criterion (AIC; 83) to verify our approach as shown in equations (4) and (5), either excluding or including a plateau value of "surviving" exclusively spontaneously active AZs, respectively.

*(4)* $surviving\ fraction(t) = exp^{-K*t}$

*(5)* $surviving\ fraction(t) = (1 - plateau) * exp^{-K*t} + plateau$

In equations (4) and (5), t is the timepoint at which survival is assessed, and K is the decay constant related to survival "half-life" (the timepoint at which half of the non-surviving AZs will have "died") as $t_{1/2} = \frac{\ln(2)}{K}$. The plateau value represents the fraction of AZs that will not "turn" from

bioRxiv preprint doi: https://doi.org/10.1101/2020.08.28.271742; this version posted August 30, 2020. The copyright holder for this preprint (which was not certified by peer review) is the author/funder, who has granted bioRxiv a license to display the preprint in perpetuity. It is made available under aCC-BY-ND 4.0 International license.

spontaneous to mixed mode regardless of further stimulation. The difference in AIC warranted the use of the more complex equation (5).

**Automated spontaneous event detection**

For the automated detection of spontaneous vesicle fusion without respect to AZ positions shown in Fig. S1-1 B-F we developed an additional set of custom MATLAB code. Single steps and results of the whole procedure on a single event are shown in Fig. S1-2. Stabilized 8-bit grey scale multipage .TIF-video files (Fig. S1-2 A) were loaded into MATLAB, where the user could then manually select an area of the video with the NMJ of interest. Using the MATLAB function *bwboundaries*, a logical mask was then generated to find all pixels within the manually selected ROI. The chosen area was then extended by 20 pixels to each side, generating a rectangular selection taken from the original video. This cropped video was then further processed by slightly reducing noise using the *medfilt3* function (Fig. S1-2 B), which smoothes noise in 3D arrays by taking the median grey value in a 3x3x3 pixel neighborhood. Next, the background was subtracted to leave only transient increases in fluorescence. For this, a maximum projection of 10 closely preceding frames was generated for every frame of the video, which was then subtracted from the current frame, where every resulting negative value was set to 0 (Fig. S1-2 C). To avoid removing parts of an event, a 'lag' of 5 frames was included before the currently observed frame, resulting in a sequence of frames from the $15^{th}$ to $6^{th}$ before the current frame for the background subtraction. Every iteration of this process resulted in a single frame that was devoid of any basal GCaMP signal and excessive noise, only leaving transient fluorescence peaks that deviated from the brightest features of the last $15^{th}$ through $6^{th}$ frames. In addition to this background-subtracted video, another one was generated with the only difference being that here, instead of the maximum projection or 10 frames, an average projection of the same 10 frames was used to subtract the

bioRxiv preprint doi: https://doi.org/10.1101/2020.08.28.271742; this version posted August 30, 2020. The copyright holder for this preprint (which was not certified by peer review) is the author/funder, who has granted bioRxiv a license to display the preprint in perpetuity. It is made available under aCC-BY-ND 4.0 International license.

background. This video was then used for the exact determination of events by a 2D-Gaussian fit as described further down. A Gaussian filter (function *imgaussfilt* with a sigma of 3 pixels) was then applied to the resulting video for further noise removal (Fig. S1-2 D). This was necessary for the next step, in which regions of connected (continuously bright) pixels above a threshold grey value of 2, and within the manual selection, were identified (Fig. S1-2 E). For each of the identified regions, the median x,y-coordinates were found and temporarily defined as the location of the event (Fig. S1-2 F). Detected events within 10 pixels of the edge of the video were removed, as they represented noise and were located outside the manual NMJ selection. A square 39x39 pixel region was then chosen around each event and a Gaussian fit was performed on a maximal projection of 6 frames (peak frame and 5 succeeding frames) of the second background-subtracted video, where the average of the 15$^{th}$ to 6$^{th}$ preceding frame was subtracted from each frame (Fig. S1-2 G), as follows. A 2D-Gaussian was simulated (the 'simulated image', Fig. S1-2 H) and fit to a maximal projection of six 39x39 px frames of an event (the 'temporary image') using equation (6):

$$(6)\ \mathrm{Gaussian}(\mathrm{x},\mathrm{y}) = A * \exp^{-\left(\frac{(x-x_0)^2}{2*c^2}+\frac{(y-y_0)^2}{2*c^2}\right)} + baseline$$

$$(7)\ FWHM = 2 * \sqrt{2 * \ln(2)} * c = 2.3548 * c$$

In equation (6), $x$ and $y$ are any of the coordinates on the image of the current event, $x_0$ and $y_0$ are the center coordinates of that image, $c$ is a non-zero variable related to the full-width at half maximum (FWHM) of the Gaussian function as shown in equation (7), and *baseline* is a background correction factor. While the separation of x- and y-spread would allow non-symmetrical Gaussian fits, these parameters were kept identical in the fit, making the spread of the Gaussian uniform in 2D. An optimization procedure with the MATLAB function *fminsearch* was

bioRxiv preprint doi: https://doi.org/10.1101/2020.08.28.271742; this version posted August 30, 2020. The copyright holder for this preprint (which was not certified by peer review) is the author/funder, who has granted bioRxiv a license to display the preprint in perpetuity. It is made available under aCC-BY-ND 4.0 International license.

used to find the best parameters for the center x,y-coordinate of the Gaussian, its amplitude, its sigma value, and the baseline. An initial value of 20 was chosen for all five parameters. As a measure of the quality of the fit, a cost function was used that calculated the difference between the temporary image and the simulated image by subtracting them. As the success of *fminsearch* depends, among other factors, on the initial parameters, the optimization was additionally repeated three times with the best fit values of the previous run. The same optimization procedure with a genetic algorithm (which is less biased regarding initial parameters) yielded the same results at vastly longer processing times.

The analysis of spontaneous event amplitudes over increasing calcium concentrations shown in Fig. S1-1 B was performed in *Mhc-myrGCaMP5G/+* larvae with the script described above at $[Ca^{2+}]_{ext.}$ of 0.4, 0.75, 1.5, 3, 6 and 12 mM in HL3 by exchanging the external solutions between recordings in one animal and taking the cell-wise mean of GCaMP signals at their peak. The nonlinear fit on the cell-wise means was performed by assuming a Hill-relationship, where binding of $Ca^{2+}$ to the sensor occurs with cooperativity $h$, and half-maximal fluorescence is reached at a concentration of $[Ca^{2+}]_{ext.}$ of $K_A$ as shown in equation (8). In that equation, $F_{max}$ is the asymptotic maximal value of fluorescence at high $[Ca^{2+}]_{ext.}$, and $C$ is a baseline correction to allow a baseline fluorescence different from 0.

$$(8)\ F([Ca^{2+}]_{ext}) = F_{max} * \frac{[Ca^{2+}]_{ext}{}^{h}}{K_A{}^{h} + [Ca^{2+}]_{ext}{}^{h}} + C$$

bioRxiv preprint doi: https://doi.org/10.1101/2020.08.28.271742; this version posted August 30, 2020. The copyright holder for this preprint (which was not certified by peer review) is the author/funder, who has granted bioRxiv a license to display the preprint in perpetuity. It is made available under aCC-BY-ND 4.0 International license.

## Data and software availability

All ImageJ and MATLAB code used in this paper will be made available by the corresponding author (A.M.W., awalter@fmp-berlin.de) upon reasonable request.

## **Author contributions** (CRediT taxonomy)

Conceptualization, A.T.G. and A.M.W.; Formal Analysis, A.T.G., A.W.M., M.J. and T.W.B.G.; Funding Acquisition, A.M.W.; Investigation, A.T.G., A.W.M., M.J. and T.W.B.G; Software, A.T.G. and A.M.W.; Supervision, A.M.W.; Visualization, A.T.G., A.W.M., M.J. and T.W.B.G; Writing – Original Draft, A.T.G. and A.M.W. Corresponding&Lead Author, A.M.W. (awalter@fmp-berlin.de)

## Acknowledgments

We thank Stephan Sigrist and Volker Haucke for helpful discussion of the manuscript. We would like to thank Sabine Hahn for excellent technical assistance. M.J. was funded by a PhD-fellowship from the Einstein Center for Neurosciences Berlin. Grants from Deutsche Forschungsgemeinschaft (DFG) included TRR186 and an Emmy-Noether grant to A.M.W.

## Competing Interests

All authors confirm the absence of any financial or non-financial competing interests.

bioRxiv preprint doi: https://doi.org/10.1101/2020.08.28.271742; this version posted August 30, 2020. The copyright holder for this preprint (which was not certified by peer review) is the author/funder, who has granted bioRxiv a license to display the preprint in perpetuity. It is made available under aCC-BY-ND 4.0 International license.

# References


1. Südhof TC. Neurotransmitter release: the last millisecond in the life of a synaptic vesicle. Neuron 2013; 80(3):675–90.

2. Fatt P, Katz B. Spontaneous subthreshold activity at motor nerve endings. J Physiol (Lond ) 1952; 117(1):109–28.

3. Kaeser PS, Regehr WG. Molecular mechanisms for synchronous, asynchronous, and spontaneous neurotransmitter release. Annu Rev Physiol 2014; 76:333–63.

4. Schneggenburger R, Rosenmund C. Molecular mechanisms governing Ca(2+) regulation of evoked and spontaneous release. Nat Neurosci 2015; 18(7):935–41.

5. Kavalali ET. The mechanisms and functions of spontaneous neurotransmitter release. Nat Rev Neurosci 2015; 16(1):5–16.

6. Littleton JT, Bellen HJ. Synaptotagmin controls and modulates synaptic-vesicle fusion in a Ca2+-dependent manner. Trends in Neurosciences 1995; 18(4):177–83.

7. Südhof TC. Calcium control of neurotransmitter release. Cold Spring Harb Perspect Biol 2012; 4(1):a011353.

8. Rizo J. Mechanism of neurotransmitter release coming into focus. Protein Sci 2018; 27(8):1364–91.

9. Jahn R, Fasshauer D. Molecular machines governing exocytosis of synaptic vesicles. Nature 2012; 490(7419):201–7.

10. Südhof TC, Rothman JE. Membrane fusion: grappling with SNARE and SM proteins. Science 2009; 323(5913):474–7.

11. Toonen RFG, Verhage M. Munc18-1 in secretion: lonely Munc joins SNARE team and takes control. Trends in Neurosciences 2007; 30(11):564–72.

12. Brose N, Rosenmund C, Rettig J. Regulation of transmitter release by Unc-13 and its homologues. Curr Opin Neurobiol 2000; 10(3):303–11.

13. Südhof TC. The presynaptic active zone. Neuron 2012; 75(1):11–25.

14. Walter AM, Böhme MA, Sigrist SJ. Vesicle release site organization at synaptic active zones. Neurosci Res 2018; 127:3–13.

15. Held RG, Kaeser PS. ELKS active zone proteins as multitasking scaffolds for secretion. Open Biol 2018; 8(2).

16. McMahon HT, Missler M, Li C, Südhof TC. Complexins: Cytosolic proteins that regulate SNAP receptor function. Cell 1995; 83(1):111–9.

17. Chen X, Tomchick DR, Kovrigin E, Araç D, Machius M, Südhof TC et al. Three-Dimensional Structure of the Complexin/SNARE Complex. Neuron 2002; 33(3):397–409.

18. Martin JA, Hu Z, Fenz KM, Fernandez J, Dittman JS. Complexin has opposite effects on two modes of synaptic vesicle fusion. Curr Biol 2011; 21(2):97–105.

19. Broadie K, Bellen HJ, DiAntonio A, Littleton JT, Schwarz TL. Absence of synaptotagmin disrupts excitation-secretion coupling during synaptic transmission. Proc Natl Acad Sci U S A 1994; 91(22):10727–31.

20. Littleton JT, Stern M, Schulze K, Perin M, Bellen HJ. Mutational analysis of Drosophila synaptotagmin demonstrates its essential role in Ca2+-activated neurotransmitter release. Cell 1993; 74(6):1125–34. Available from: URL: http://www.sciencedirect.com/science/article/pii/0092867493907337.

21. Hobson RJ, Liu Q, Watanabe S, Jorgensen EM. Complexin maintains vesicles in the primed state in C. elegans. Curr Biol 2011; 21(2):106–13.

22. Huntwork S, Littleton JT. A complexin fusion clamp regulates spontaneous neurotransmitter release and synaptic growth. Nat Neurosci 2007; 10(10):1235–7.

23. Bacaj T, Wu D, Yang X, Morishita W, Zhou P, Xu W et al. Synaptotagmin-1 and synaptotagmin-7 trigger synchronous and asynchronous phases of neurotransmitter release. Neuron 2013; 80(4):947–59.

24. Kerr AM, Reisinger E, Jonas P. Differential dependence of phasic transmitter release on synaptotagmin 1 at GABAergic and glutamatergic hippocampal synapses. Proc Natl Acad Sci U S A 2008; 105(40):15581–6.

25. Wierda KDB, Sørensen JB. Innervation by a GABAergic neuron depresses spontaneous release in glutamatergic neurons and unveils the clamping phenotype of synaptotagmin-1. Journal of Neuroscience 2014; 34(6):2100–10.

26. Reim K, Mansour M, Varoqueaux F, McMahon HT, Südhof TC, Brose N et al. Complexins Regulate a Late Step in Ca2+-Dependent Neurotransmitter Release. Cell 2001; 104(1):71–81.

27. Yang X, Cao P, Südhof TC. Deconstructing complexin function in activating and clamping Ca2+-triggered exocytosis by comparing knockout and knockdown phenotypes. Proc Natl Acad Sci U S A 2013; 110(51):20777–82.

28. Geppert M, Goda Y, Hammer RE, Li C, Rosahl TW, Stevens CF et al. Synaptotagmin I: A major Ca2+ sensor for transmitter release at a central synapse. Cell 1994; 79(4):717–27.

29. López-Murcia FJ, Reim K, Jahn O, Taschenberger H, Brose N. Acute Complexin Knockout Abates Spontaneous and Evoked Transmitter Release. Cell Rep 2019; 26(10):2521-2530.e5.

30. Arancillo M, Min S-W, Gerber S, Münster-Wandowski A, Wu Y-J, Herman M et al. Titration of Syntaxin1 in mammalian synapses reveals multiple roles in vesicle docking, priming, and release probability. Journal of Neuroscience 2013; 33(42):16698–714.

31. Weber JP, Reim K, Sørensen JB. Opposing functions of two sub-domains of the SNARE-complex in neurotransmission. EMBO J 2010; 29(15):2477–90.

32. Courtney NA, Briguglio JS, Bradberry MM, Greer C, Chapman ER. Excitatory and Inhibitory Neurons Utilize Different Ca2+ Sensors and Sources to Regulate Spontaneous Release. Neuron 2018; 98(5):977-991.e5.

33. Groffen AJ, Martens S, Díez Arazola R, Cornelisse LN, Lozovaya N, Jong APH de et al. Doc2b is a high-affinity Ca2+ sensor for spontaneous neurotransmitter release. Science 2010; 327(5973):1614–8.

34. Pang ZP, Bacaj T, Yang X, Zhou P, Xu W, Südhof TC. Doc2 supports spontaneous synaptic transmission by a

bioRxiv preprint doi: https://doi.org/10.1101/2020.08.28.271742; this version posted August 30, 2020. The copyright holder for this preprint (which was not certified by peer review) is the author/funder, who has granted bioRxiv a license to display the preprint in perpetuity. It is made available under aCC-BY-ND 4.0 International license.

Ca(2+)-independent mechanism. Neuron 2011; 70(2):244–51.

35. Ramirez DMO, Khvotchev M, Trauterman B, Kavalali ET. Vti1a identifies a vesicle pool that preferentially recycles at rest and maintains spontaneous neurotransmission. Neuron 2012; 73(1):121–34.

36. Bal M, Leitz J, Reese AL, Ramirez DMO, Durakoglugil M, Herz J et al. Reelin mobilizes a VAMP7-dependent synaptic vesicle pool and selectively augments spontaneous neurotransmission. Neuron 2013; 80(4):934–46.

37. Deitcher DL, Ueda A, Stewart BA, Burgess RW, Kidokoro Y, Schwarz TL. Distinct Requirements for Evoked and Spontaneous Release of Neurotransmitter Are Revealed by Mutations in the Drosophila Gene neuronal-synaptobrevin. J Neurosci 1998; 18(6):2028–39.

38. Schoch S, Deák F, Königstorfer A, Mozhayeva M, Sara Y, Südhof TC et al. SNARE function analyzed in synaptobrevin/VAMP knockout mice. Science 2001; 294(5544):1117–22.

39. Broadie K, Prokop A, Bellen HJ, O'Kane CJ, Schulze KL, Sweeney ST. Syntaxin and synaptobrevin function downstream of vesicle docking in drosophila. Neuron 1995; 15(3):663–73.

40. Guerrero G, Reiff DF, Rieff DF, Agarwal G, Ball RW, Borst A et al. Heterogeneity in synaptic transmission along a Drosophila larval motor axon. Nat Neurosci 2005; 8(9):1188–96.

41. Melom JE, Akbergenova Y, Gavornik JP, Littleton JT. Spontaneous and evoked release are independently regulated at individual active zones. J Neurosci 2013; 33(44):17253–63.

42. Peled ES, Newman ZL, Isacoff EY. Evoked and spontaneous transmission favored by distinct sets of synapses. Curr Biol 2014; 24(5):484–93.

43. Muhammad K, Reddy-Alla S, Driller JH, Schreiner D, Rey U, Böhme MA et al. Presynaptic spinophilin tunes neurexin signalling to control active zone architecture and function. Nat Commun 2015; 6:8362.

44. Xu J, Pang ZP, Shin O-H, Südhof TC. Synaptotagmin-1 functions as a Ca2+ sensor for spontaneous release. Nat Neurosci 2009; 12(6):759–66.

45. Lou X, Scheuss V, Schneggenburger R. Allosteric modulation of the presynaptic Ca2+ sensor for vesicle fusion. Nature 2005; 435(7041):497–501.

46. Llano I, González J, Caputo C, Lai FA, Blayney LM, Tan YP et al. Presynaptic calcium stores underlie large-amplitude miniature IPSCs and spontaneous calcium transients. Nat Neurosci 2000; 3(12):1256–65.

47. Emptage NJ, Reid CA, Fine A. Calcium Stores in Hippocampal Synaptic Boutons Mediate Short-Term Plasticity, Store-Operated Ca2+ Entry, and Spontaneous Transmitter Release. Neuron 2001; 29(1):197–208.

48. Ermolyuk YS, Alder FG, Surges R, Pavlov IY, Timofeeva Y, Kullmann DM et al. Differential triggering of spontaneous glutamate release by P/Q-, N- and R-type Ca2+ channels. Nat Neurosci 2013; 16(12):1754–63.

49. Goswami SP, Bucurenciu I, Jonas P. Miniature IPSCs in hippocampal granule cells are triggered by voltage-gated Ca2+ channels via microdomain coupling. Journal of Neuroscience 2012; 32(41):14294–304.

50. Shahrezaei V, Cao A, Delaney KR. Ca2+ from one or two channels controls fusion of a single vesicle at the frog neuromuscular junction. J Neurosci 2006; 26(51):13240–9.

51. Goel P, Li X, Dickman D. Disparate Postsynaptic Induction Mechanisms Ultimately Converge to Drive the Retrograde Enhancement of Presynaptic Efficacy. Cell Rep 2017; 21(9):2339–47.

52. Groemer TW, Klingauf J. Synaptic vesicles recycling spontaneously and during activity belong to the same vesicle pool. Nat Neurosci 2007; 10(2):145–7.

53. Hua Y, Sinha R, Martineau M, Kahms M, Klingauf J. A common origin of synaptic vesicles undergoing evoked and spontaneous fusion. Nat Neurosci 2010; 13(12):1451–3.

54. Wilhelm BG, Groemer TW, Rizzoli SO. The same synaptic vesicles drive active and spontaneous release. Nat Neurosci 2010; 13(12):1454–6.

55. Fredj NB, Burrone J. A resting pool of vesicles is responsible for spontaneous vesicle fusion at the synapse. Nat Neurosci 2009; 12(6):751–8.

56. Koenig JH, Ikeda K. Contribution of active zone subpopulation of vesicles to evoked and spontaneous release. J Neurophysiol 1999; 81(4):1495–505.

57. Sara Y, Virmani T, Deák F, Liu X, Kavalali ET. An isolated pool of vesicles recycles at rest and drives spontaneous neurotransmission. Neuron 2005; 45(4):563–73.

58. Atasoy D, Ertunc M, Moulder KL, Blackwell J, Chung C, Su J et al. Spontaneous and evoked glutamate release activates two populations of NMDA receptors with limited overlap. J Neurosci 2008; 28(40):10151–66.

59. Sara Y, Bal M, Adachi M, Monteggia LM, Kavalali ET. Use-dependent AMPA receptor block reveals segregation of spontaneous and evoked glutamatergic neurotransmission. J Neurosci 2011; 31(14):5378–82.

60. Frank CA, Kennedy MJ, Goold CP, Marek KW, Davis GW. Mechanisms underlying the rapid induction and sustained expression of synaptic homeostasis. Neuron 2006; 52(4):663–77.

61. Reese AL, Kavalali ET. Single synapse evaluation of the postsynaptic NMDA receptors targeted by evoked and spontaneous neurotransmission. Elife 2016; 5.

62. Peled ES, Isacoff EY. Optical quantal analysis of synaptic transmission in wild-type and rab3-mutant Drosophila motor axons. Nat Neurosci 2011; 14(4):519–26.

63. Kittel RJ, Wichmann C, Rasse TM, Fouquet W, Schmidt M, Schmid A et al. Bruchpilot promotes active zone assembly, Ca2+ channel clustering, and vesicle release. Science 2006; 312(5776):1051–4.

64. Reddy-Alla S, Böhme MA, Reynolds E, Beis C, Grasskamp AT, Mampell MM et al. Stable Positioning of Unc13 Restricts Synaptic Vesicle Fusion to Defined Release Sites to Promote Synchronous Neurotransmission. Neuron 2017; 95(6):1350-1364.e12.

65. Hou J, Tamura T, Kidokoro Y. Delayed synaptic transmission in Drosophila cacophonynull embryos. J Neurophysiol 2008; 100(5):2833–42.

bioRxiv preprint doi: https://doi.org/10.1101/2020.08.28.271742; this version posted August 30, 2020. The copyright holder for this preprint (which was not certified by peer review) is the author/funder, who has granted bioRxiv a license to display the preprint in perpetuity. It is made available under aCC-BY-ND 4.0 International license.

66. Gratz SJ, Goel P, Bruckner JJ, Hernandez RX, Khateeb K, Macleod GT et al. Endogenous Tagging Reveals Differential Regulation of Ca2+ Channels at Single Active Zones during Presynaptic Homeostatic Potentiation and Depression. J Neurosci 2019; 39(13):2416–29.

67. Akbergenova Y, Cunningham KL, Zhang YV, Weiss S, Littleton JT. Characterization of developmental and molecular factors underlying release heterogeneity at Drosophila synapses. Elife 2018; 7.

68. Brenner S. The Genetics of CAENORHABDITIS ELEGANS. Genetics 1974; 77(1):71–94.

69. Dittman JS. Unc13: a multifunctional synaptic marvel. Curr Opin Neurobiol 2019; 57:17–25.

70. Böhme MA, Grasskamp AT, Walter AM. Regulation of synaptic release-site Ca2+ channel coupling as a mechanism to control release probability and short-term plasticity. FEBS Lett 2018; 592(21):3516–31.

71. Rizo J, Rosenmund C. Synaptic vesicle fusion. Nat Struct Mol Biol 2008; 15(7):665–74.

72. Richmond JE, Broadie KS. The synaptic vesicle cycle: exocytosis and endocytosis in Drosophila and C. elegans. Curr Opin Neurobiol 2002; 12(5):499–507.

73. Sakamoto H, Ariyoshi T, Kimpara N, Sugao K, Taiko I, Takikawa K et al. Synaptic weight set by Munc13-1 supramolecular assemblies. Nat Neurosci 2018; 21(1):41–9.

74. Kobbersmed JRL, Grasskamp AT, Jusyte M, Böhme MA, Ditlevsen S, Sørensen JB et al. Rapid regulation of vesicle priming explains synaptic facilitation despite heterogeneous vesicle:Ca2+ channel distances. Elife 2020; 9.

75. Böhme MA, Beis C, Reddy-Alla S, Reynolds E, Mampell MM, Grasskamp AT et al. Active zone scaffolds differentially accumulate Unc13 isoforms to tune Ca(2+) channel-vesicle coupling. Nat Neurosci 2016; 19(10):1311–20.

76. Yoshihara M, Adolfsen B, Littleton JT. Is synaptotagmin the calcium sensor? Curr Opin Neurobiol 2003; 13(3):315–23.

77. Koh T-W, Bellen HJ. Synaptotagmin I, a Ca2+ sensor for neurotransmitter release. Trends in Neurosciences 2003; 26(8):413–22.

78. Fouquet W, Owald D, Wichmann C, Mertel S, Depner H, Dyba M et al. Maturation of active zone assembly by Drosophila Bruchpilot. J Cell Biol 2009; 186(1):129–45.

79. Ryglewski S, Lance K, Levine RB, Duch C. Ca(v)2 channels mediate low and high voltage-activated calcium currents in Drosophila motoneurons. J Physiol (Lond ) 2012; 590(4):809–25.

80. Vyleta NP, Smith SM. Spontaneous Glutamate Release Is Independent of Calcium Influx and Tonically Activated by the Calcium-Sensing Receptor. Journal of Neuroscience 2011; 31(12):4593–606.

81. Davis GW, Müller M. Homeostatic control of presynaptic neurotransmitter release. Annu Rev Physiol 2015; 77:251–70.

82. Harris KP, Littleton JT. Transmission, Development, and Plasticity of Synapses. Genetics 2015; 201(2):345–75.

83. Akaike H. A new look at the statistical model identification. IEEE Trans. Automat. Contr. 1974; 19(6):716–23.

84. Zefirov A, Benish T, Fatkullin N, Cheranov S, Khazipov R. Localization of active zones. Nature 1995; 376(6539):393–4.

85. Alabi AA, Tsien RW. Synaptic vesicle pools and dynamics. Cold Spring Harb Perspect Biol 2012; 4(8):a013680.

86. Walter AM, Haucke V, Sigrist SJ. Neurotransmission: spontaneous and evoked release filing for divorce. Curr Biol 2014; 24(5):R192-4.

87. Truckenbrodt S, Rizzoli SO. Spontaneous vesicle recycling in the synaptic bouton. Front Cell Neurosci 2014; 8:409.

88. Sigrist SJ, Reiff DF, Thiel PR, Steinert JR, Schuster CM. Experience-dependent strengthening of Drosophila neuromuscular junctions. J Neurosci 2003; 23(16):6546–56.

89. Qin G, Schwarz T, Kittel RJ, Schmid A, Rasse TM, Kappei D et al. Four different subunits are essential for expressing the synaptic glutamate receptor at neuromuscular junctions of Drosophila. J Neurosci 2005; 25(12):3209–18.

90. Stewart B, Atwood HL, Renger JJ, Wang J, Wu CF. Improved stability of Drosophila larval neuromuscular preparations in haemolymph-like physiological solutions. J Comp Physiol A 1994; 175(2):179–91.

91. Zhang B, Stewart B. Electrophysiological recording from Drosophila larval body-wall muscles. Cold Spring Harb Protoc 2010; 2010(9):pdb.prot5487.

92. Ullrich A, Böhme MA, Schöneberg J, Depner H, Sigrist SJ, Noé F. Dynamical Organization of Syntaxin-1A at the Presynaptic Active Zone. PLoS Comput Biol 2015; 11(9):e1004407.

93. Thévenaz P, Ruttimann UE, Unser M. A pyramid approach to subpixel registration based on intensity. IEEE Trans Image Process 1998; 7(1):27–41.